Title
K-p INTERACTIONS AROUND 1 BeV/c AND THE Y*0 (l8l5)

Permalink
https://escholarship.org/uc/item/18w184xz

Author
Sahouria, Jack Yacoub S.

Publication Date
1969

UCRL-18624
c.2

K$^-$p INTERACTIONS AROUND 1 BeV/c AND THE $Y_0^*(1815)$

Jack Yacoub S. Sahouria
(Ph. D. Thesis)

January 1969

LAWRENCE RADIATION LABORATORY
UNIVERSITY of CALIFORNIA BERKELEY

DISCLAIMER

UCRL-18624

UNIVERSITY OF CALIFORNIA

Lawrence Radiation Laboratory
Berkeley, California

AEC Contract No. W-7405-eng-48

K^-p INTERACTIONS AROUND 1 BeV/c AND THE $Y_0^*(1815)$

Jack Yacoub S. Sahouria
(Ph. D. Thesis)

January 1969

K^-p INTERACTIONS AROUND 1 BEV/C AND THE $Y_0^*(1815)$

Contents

K^-p INTERACTIONS AROUND 1 BEV/C AND THE $Y_0^*(1815)$

Jack Yacoub S. Sahouria

Lawrence Radiation Laboratory
University of California
Berkeley, California

November 1968

ABSTRACT

The reaction $K^-p \rightarrow \Lambda\,\pi^+\pi^-$ in the center-of-mass energy range 1700 to 1850 MeV is analyzed under the assumption, which is well substantiated by the data, that the reaction proceeds mainly by the production of the intermediate state $Y_1^*(1385)$. A good fit to the production and decay angular distributions and the mass plots of the $Y_1^{*\pm}(1385)$ and the lambda polarization is obtained, showing the well known resonances $Y_1^*(1770)$ and the $Y_0^*(1820)$. This fit also requires a possibly resonating state with iso-spin, spin and parity $0(3/2^+)$ and mass at or below 1700 MeV which is the low end of the energy range in this experiment. The branching fractions of the states $Y_1^*(1770)$ and $Y_0^*(1820)$ into the final state $Y_1^{*\pm}(1385) + \pi^\mp$ are found to be (8.0 ± 3.3) per cent and (8.0 ± 1.4) per cent respectively; and the phase between these two states is (201 ± 14), (136 ± 19) and (167 ± 25) degrees at the center-of-mass energies 1803, 1821 and 1846 MeV respectively. The masses of the Y_1^{*+} and $Y_1^{*-}(1385)$ and the mass difference $(Y_1^{*-} - Y_1^{*+})$ are obtained as (1384.2 ± 1.4) MeV, (1387.8 ± 1.2) MeV and (3.6 ± 1.0) MeV respectively. The interference between the iso-spin states 0 and 1 explains the difference between the production rates of the $Y_1^{*+}(1385)$ and the $Y_1^{*-}(1385)$ in the above reaction.

I. INTRODUCTION

The cross-section measurements by various investigators[1a] of the reactions in the K^-p and K^-n system showed structures which were not completely understood at first. The K^-p total cross-section showed a rise near the center-of-mass energy 1815 MeV, and the elastic differential cross-section could only be fit by using Legendre-polynomials up to 5th order in a partial wave fit.[1a] This motivated the Powell-Birge group at the Lawrence Radiation Laboratory to perform an experiment at the Bevatron in 1964. Approximately 250 000 pictures were taken in the 25 inch Hydrogen Bubble Chamber with the K^- momenta ranging from 820 to 1113 MeV/c. Other groups at C.E.R.N. and the University of Maryland started similar experiments at approximately the same time. As a result, these reactions have been closely studied during the past several years and a number of results have emerged,[34] new resonances were discovered and others which had been suggested previously were confirmed, in particular the $Y_1^*(1765)$ and the $Y_0^*(1815)$.

In this experiment one of the event-types scanned for was the three-particle final state $K^-p \rightarrow \Lambda \pi^+\pi^-$. This channel contains the iso-spin states 0 and 1, and can be the final state decay product of both Y_0^* and Y_1^* resonances produced in the K^-p collision. Indeed the distribution of events on a Dalitz plot shows an asymmetry in favor of the negatively charged $\Lambda\pi$ state. This asymmetry can only come from the interference of the two iso-spin amplitudes in the final state. A systematic study of this channel should resolve some of the ambiguities that arise in studying partial cross-sections, or channels which are only in one isotopic spin state. Moreover, the branching ratios of established resonances into this channel would be useful in theoretical considerations.

This report will be in three major parts. First, there will be a description of the experimental arrangement, scanning, measuring and selection of the data. Then there is a formulation of the model used to make a fit to the data and finally the measured quantities and the fits to the model will be discussed.

II. DETAILS OF EXPERIMENT AND DATA PROCESSING

A. Experimental Procedure

1. The beam

In the Fall of 1963 a two stage, variable momentum separated $K^{\pm}$ beam was constructed at the Bevatron, using a copper target 0.35 inch wide, 4.0 inch long and 0.15 inch high placed in the external proton beam.[1] It was capable of being tuned for the range of momenta 800 - 1150 MeV/c for K^- and 800 - 1600 MeV/c for K^+ giving a reasonable flux at the bubble chamber. The beam consisted of nine quadropole magnets, four bending magnets, two parallel-plate spectrometers, two mass-separation slits and a Uranium collimator with variable horizontal aperture 0.0 to 5.0 inches.

Some of the features of the beam are: (under the mode of operation for this experiment)

a. Short length, 1115 inches target to chamber (3.15 K^- decay lengths at 1200 MeV/c K^- momentum).

b. Large horizontal and vertical acceptance of 130.0 and 6.8 milliradians respectively.

c. Large ratio of K-π separation to image size: 0.25 inches/0.09 inches at the first slit; and 0.28 inches/0.09 inches at the second slit. (These numbers are for 1200 MeV/c K momentum).

d. Relatively small total momentum bite of 2%.

The 25 inch LRL hydrogen bubble chamber was used as a detector. Exposures were made at seven nominal values of K^- momentum: 850, 900, 950, 1000, 1050, 1100, 1150 MeV/c. The average number of tracks per picture ranged from 8 to 15 for a low intensity exposure and from 15 to 25 for a high intensity exposure. The total number of pictures taken was approximately 0.4 million. Two short exposures of approximately 10 000 pictures each were made at the nominal momenta 925 and 975 MeV/c.

The magnetic field in the bubble chamber ranged from 16 443 to 18 531 Gauss.

2. Scanning and Measurement

We scanned 144 rolls containing approximately 3.02×10^6 tracks. The scanners were instructed to record all interactions where a neutral decaying into a (V) is pointing towards an origin with two outgoing prongs, see Fig. 1. Of course the same V may be pointing towards two different origins, or two V's may point towards the same origin. All of these were recorded. This ambiguity will be discussed in the section on bookkeeping. We have rescanned 141 rolls and any differences between the two scans were checked on the scan table by a graduate student leading to an average scan efficiency of 94.9 per cent.

We used the Flying Spot Digitizer (FSD) to measure 133 rolls,[2] the rest and any event that failed a second remeasure on the FSD was measured on a microscope or a Franckenstein. The most common failures on the FSD are the events obstructed by other crossing tracks, and events which have tracks or fiducial marks fainter then a certain level. Events that failed a third measurement (1.2% of the total) were rejected. The Fog-Cloudy-Fair system was used to reconstruct tracks in space (FOG) and constrain the events to the following hypotheses (CLOUDY):

$$\begin{aligned} K^- p &\rightarrow \Lambda \pi^+ \pi^- \\ &\rightarrow \Lambda \pi^+ \pi^- \pi^0 \\ &\rightarrow \bar{K}^0 p \pi^- \end{aligned}$$

In this report we are concerned with the first hypothesis only $(\Lambda \pi^+ \pi^-)$.

For the purposes of constraint, we edited the beam momenta. This was done by measuring long beam tracks to determine the central value

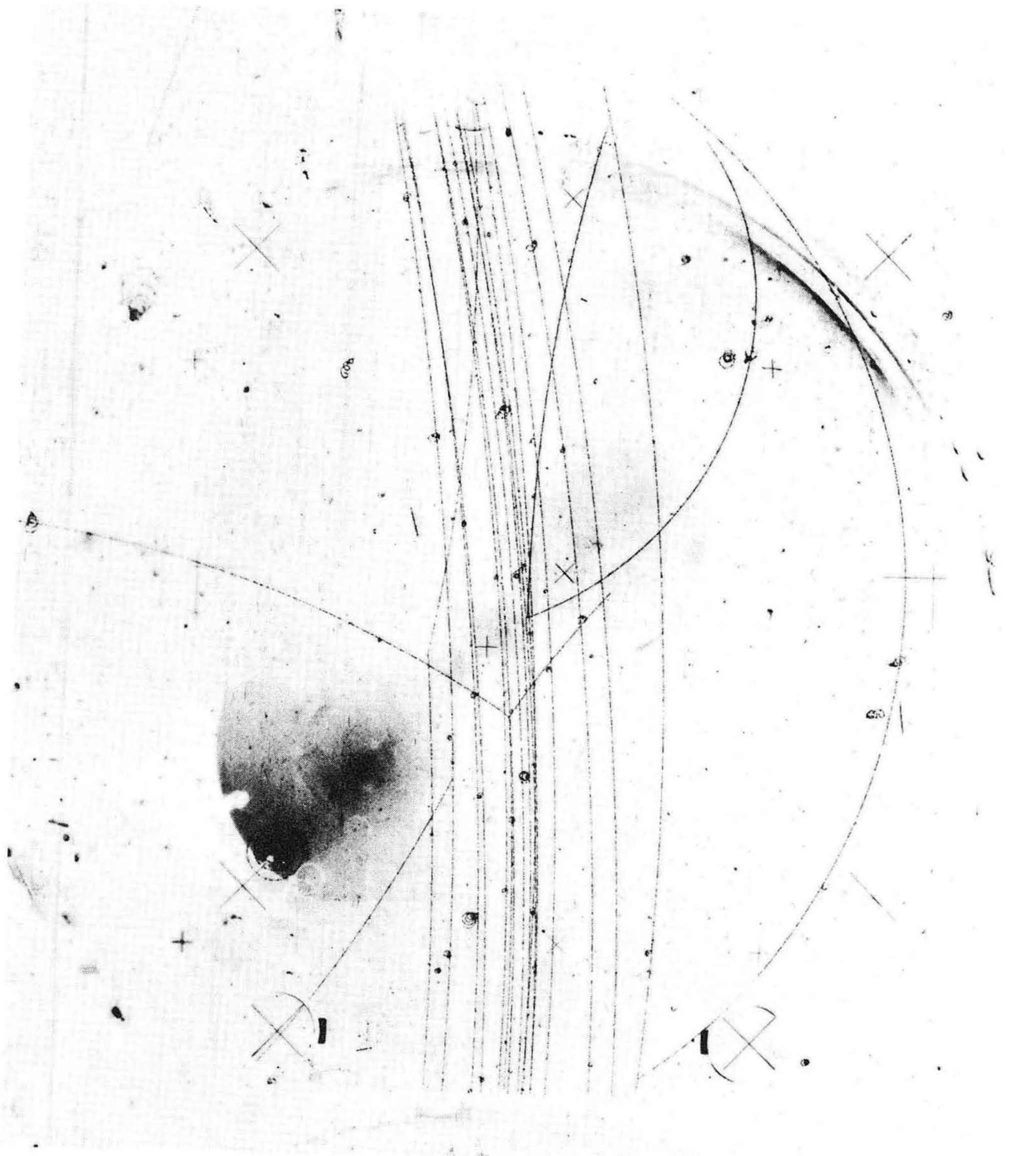

XBB 6811-6986

Fig. 1

of the momentum distribution and its width. The edited values obtained were 822, 878, 900, 924, 950, 975, 1020, 1058, 1113, for the nominal values of the momenta 850, 900, 925, 950, 975, 1000, 1050, 1100, 1150 respectively. The error on the edited momentum was assumed to be ~3% in the constraining routines.

3. Bookkeeping

We have written a series of computer programs to do the bookkeeping on these data. The method is the following:

a. Put all the events scanned on tape ordered by roll and frame number (scan tape).

b. Compare the scan tape with a list of the events that have passed the reconstruction program and with a list of the events that passed the kinematical constraining program, and make a final list that contains all this information.

c. Scan this final list and extract the following information:

   1) Gaps in frame number that contain no recorded events and verify on scan table, and the beginning and the end of rolls to make sure that no events have been lost during the data handling operation.

   2) Events on one frame that have a common interaction origin but with different V's or vice versa.

   3) Check if there are more than one entry for the same event (remeasures) and save this information on the final list.

d. The final list is scanned again; rolls or section of rolls that contain events that got lost in the system are recorded (for purposes of cross-section measurement), ambiguous events (see c above) are resolved by choosing the one that gives lower chi squared in the kinematic constraint.

4. Beam Normalization

a. Beam track count: We counted the number of tracks per frame every 25 frames on 141 rolls of film. As opposed to the usual way of measuring track length by counting τ ($K\pi_3$) decays, this method though lengthy gives a higher precision. Our purpose was to eliminate tracks of particles which passed through an obstruction, did not pass through the thin beam window or interacted outside the chamber.in order to make a partial cross-section measurement. The decision that a certain track is or is not a "beam track" was made with the aid of a template made for this purpose. Fourteen templates were made, one for each setting of the chamber magnet and each value of the magnification of the scan tables on which the templates were used. These templates were made (based on a small sample of film) by measuring the difference in lateral position in the beam plane (the horizontal plane) between two different points on a track. If we imagine that the beam-axis is a Z-axis and the X-Z plane is horizontal, then the region of "good" beam tracks on these templates corresponds to a range in azimuthal angle 10° - 14° projected on the X-Z plane. An average of 3.6% of the tracks are rejected as non-beam tracks. The beam counts made by different scanners are 99.5 - 99.9% consistent. The average number of tracks per frame ranges from 8 to 27 on different rolls of film. See Table I.

b. Pion and Muon Contamination - The K^- beam in the chamber is contaminated with pions and muons that are products of decay or interaction of K^-'s outside the chamber or pions coming directly from target. A simple method for estimating this contamination

Table I. Data for partial cross-section measurement. The correction for scan efficiency and Σ^0 contamination in $K^-p \rightarrow \Lambda\pi\pi$ is 5.6%.

Momentum (MeV/c)	822	878	901	924	950	975	1020	1058	1113
Invariant mass (GeV)	1.710	1.736	1.747	1.758	1.770	1.782	1.803	1.821	1.846
Weighted events	209	470	276	1301	243	1595	1375	828	544
Contamination %	4.9	5.0	6.3	6.0	6.6	6.0	5.3	9.2	9.2
Total K^- tracks x 10^3	86.27	190.75	106.60	548.28	94.03	591.05	482.40	270.40	200.65
Attenuation correction	1.053	1.042	1.052	1.053	1.053	1.053	1.056	1.052	1.047
$\sigma(\Lambda\pi^+\pi^-)$ m.b.	3.32	3.33	3.79	3.25	3.53	3.70	3.89	4.18	3.69
±	.23	.15	.25	.09	.23	.09	.11	.15	.16
Estimated number of $\Sigma^0\pi^+\pi^-$ events	18	58	30	167	24	219	168	110	97
$\sigma(\Sigma^0\pi^+\pi^-)$ m.b.	.2	.27	.25	.28	.23	.34	.32	.37	.44
±	.07	.05	.07	.03	.07	.04	.04	.05	.07

is by counting delta-rays (resulting from elastic collisions of incident particles with atomic electrons). The basis for this procedure is that at incident momenta in this experiment pions and muons can produce delta rays with momentum larger than the maximum of delta rays produced by K^- particles.[4,5] We have chosen 28 rolls of film representative both of the different momenta and the span of time over which the film was exposed, and we have scanned these for delta-rays inside a suitable fiducial volume. The delta rays are recorded if they have a diameter (momentum) on the scan table which is larger than the maximum that a K^- can produce at the incident momentum of the beam. We find that the contamination ranges from 3.87 to 11.14% and consists of 15% pions and 85% muons. See Table I.

B. The Partial Cross-Section

1. Selection of Sample

In selecting our sample of $K^-p \rightarrow \Lambda \pi^+\pi^-$ events from all the measured V and 2-prong events we make chi-square cuts on the V which correspond to a 3% probability level that the V is a lambda independent of its production origin, and 1% probability that the lambda points to the interaction origin. (See Appendix A).

To eliminate contamination from events that have an extra π^0, we used the measured momenta of the tracks, and a lambda mass of 1.1154 BeV, to study the missing mass squared $(MM1)^2$ in $(K^-p \rightarrow \Lambda \pi^+\pi^- + MM1)$, see Fig. 2a. This distribution peaks below zero as is well known and shows the π^0 peak. We accept events that give a value for $(MM1)^2$ in the range -0.012 to $+0.016$ $(BeV)^2$.

Similarily to eliminate the Σ^0 contamination from the reaction

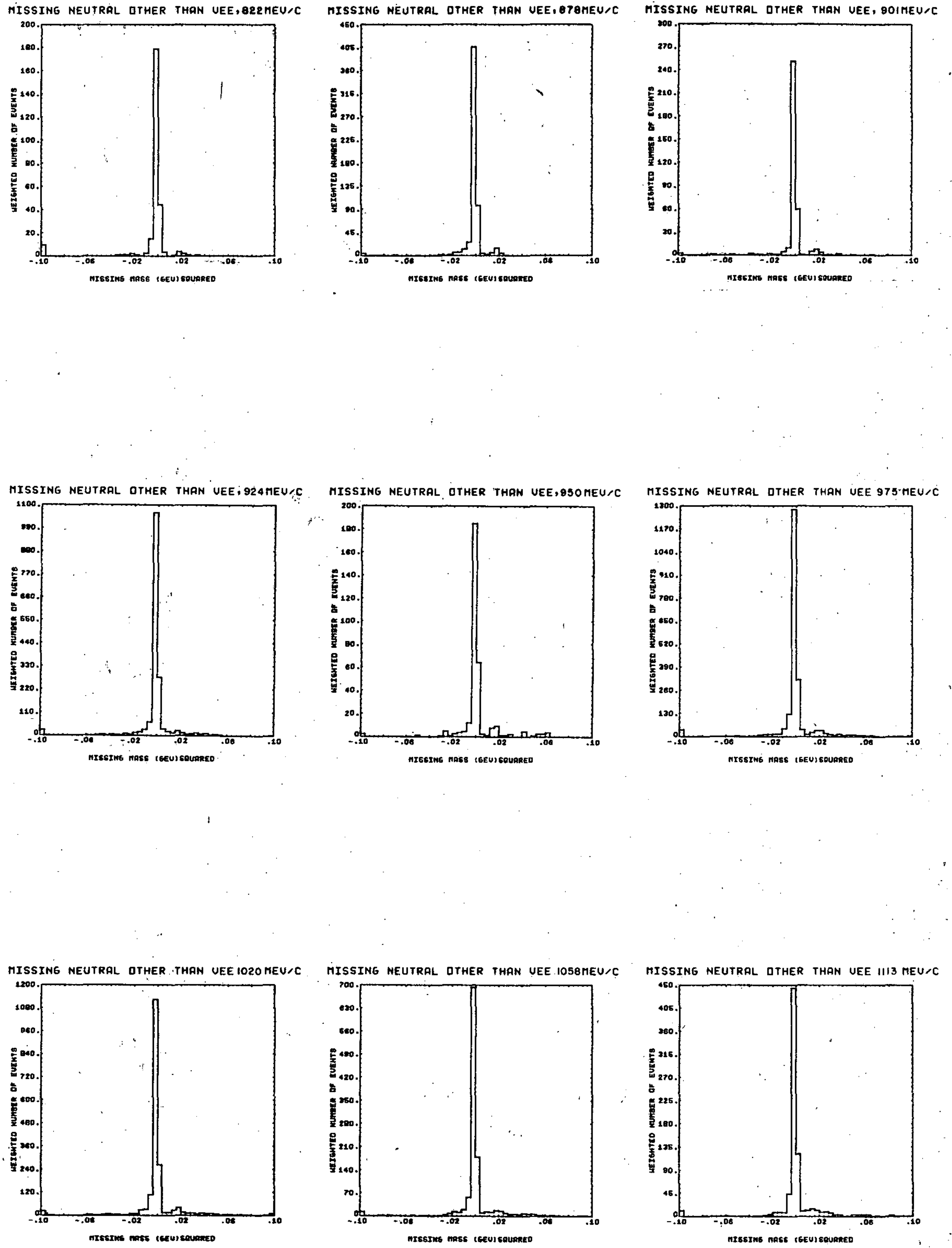

XBL 6811-6154

Fig. 2A

$$K^-p \to \Sigma^0 \pi^+\pi^- \to \Lambda\gamma\, \pi^+\pi^-$$

we studied the missing mass distribution (MM2) in ($K^-p \to \pi^+\pi^- +$ MM2), see Fig. 2b. This distribution shows well-resolved Σ^0 and Λ peaks at all momenta. Here again we used the measured values for momenta of particles to make these distributions. In order to resolve the Σ^0 and Λ peaks in the superposition region, we have studied a sample of events which are very well constrained to the hypothesis $K^-p \to \Lambda\, \pi^+\pi^-$. For this sample we found the distribution of the missing mass at the first origin (MM2) using the measured values of track momenta. This distribution shows a lambda peak with a tail in the Σ^0 region, but no Σ^0 peak. Using this sample distribution (one for each momentum), we made two distributions, one for the Λ centered at the Λ-mass and one for the Σ^0 centered at the Σ^0 mass such that when we add these two they will correspond to the total number of events at each momentum. Figure 3 is a plot of the superposition of these two curves on a (MM2) histogram for one momentum. An event is accepted if it gives a missing mass (MM2) in the range 1.02 to 1.18 BeV. Due to this selection we estimate that the Σ^0 contamination is reduced to 0.7% and that the Λ sample is depleted by 1 to 2% due to the tail of Λ peak in the Σ region.

There is an ambiguity that arises from the reaction $K^-p \to \bar{K}^0 p\, \pi^-$ which for a certain combination of track momenta can be confused with the reaction $K^-p \to \Lambda\, \pi^+\pi^-$. Thus we add an extra precaution by accepting into our sample events which have a vee that constrains neither to a Λ (3% level) nor to a $\bar{K}^0$, but converges as a Λ in the one-constraint fit at the vee vertex, and at the same time satisfies all the conditions above. Based on a study of a small sample of data we estimate the $\bar{K}^0$ contamination after the above cuts to be 0.3%. This is small primarily

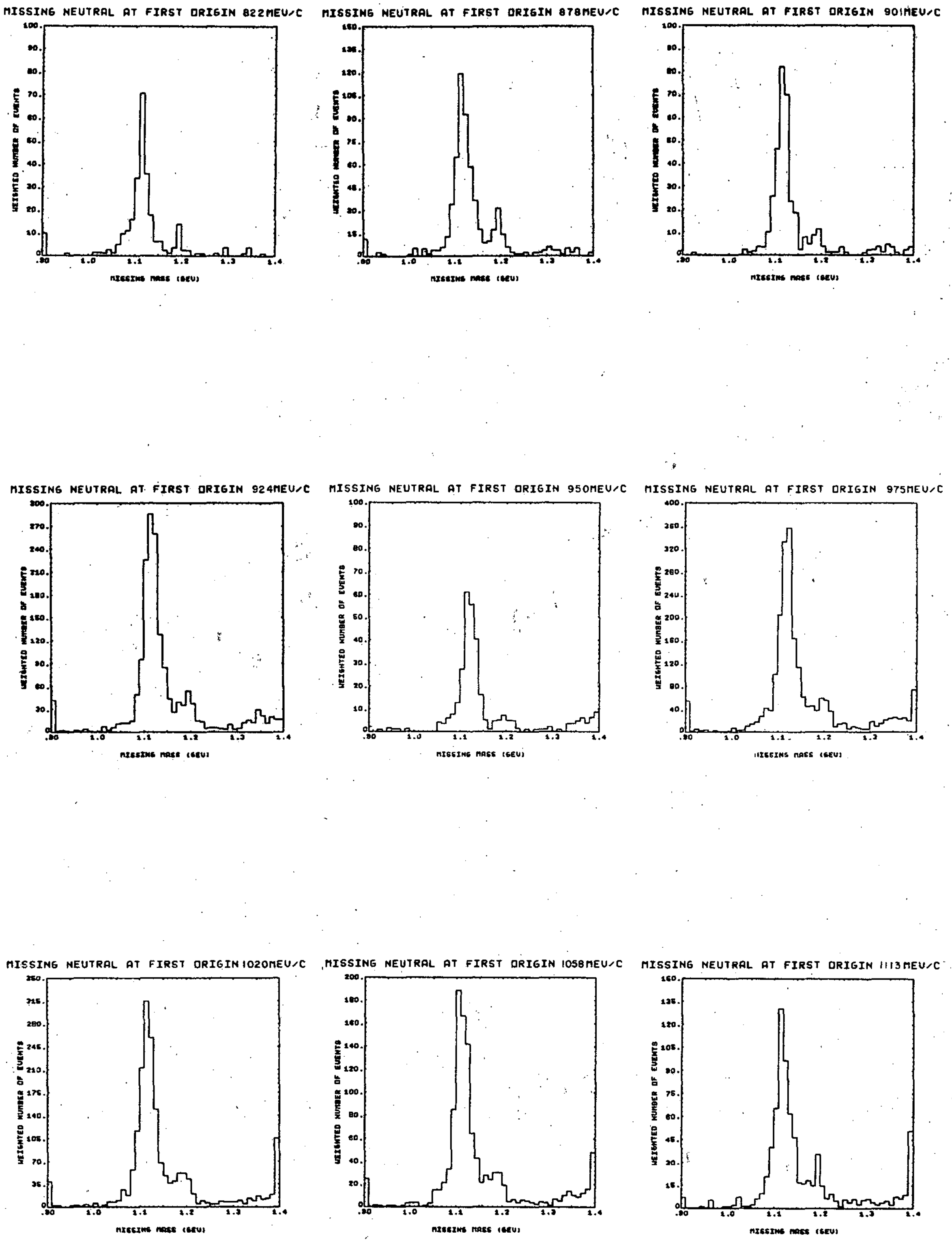

XBL 6811-6149

Fig. 2B

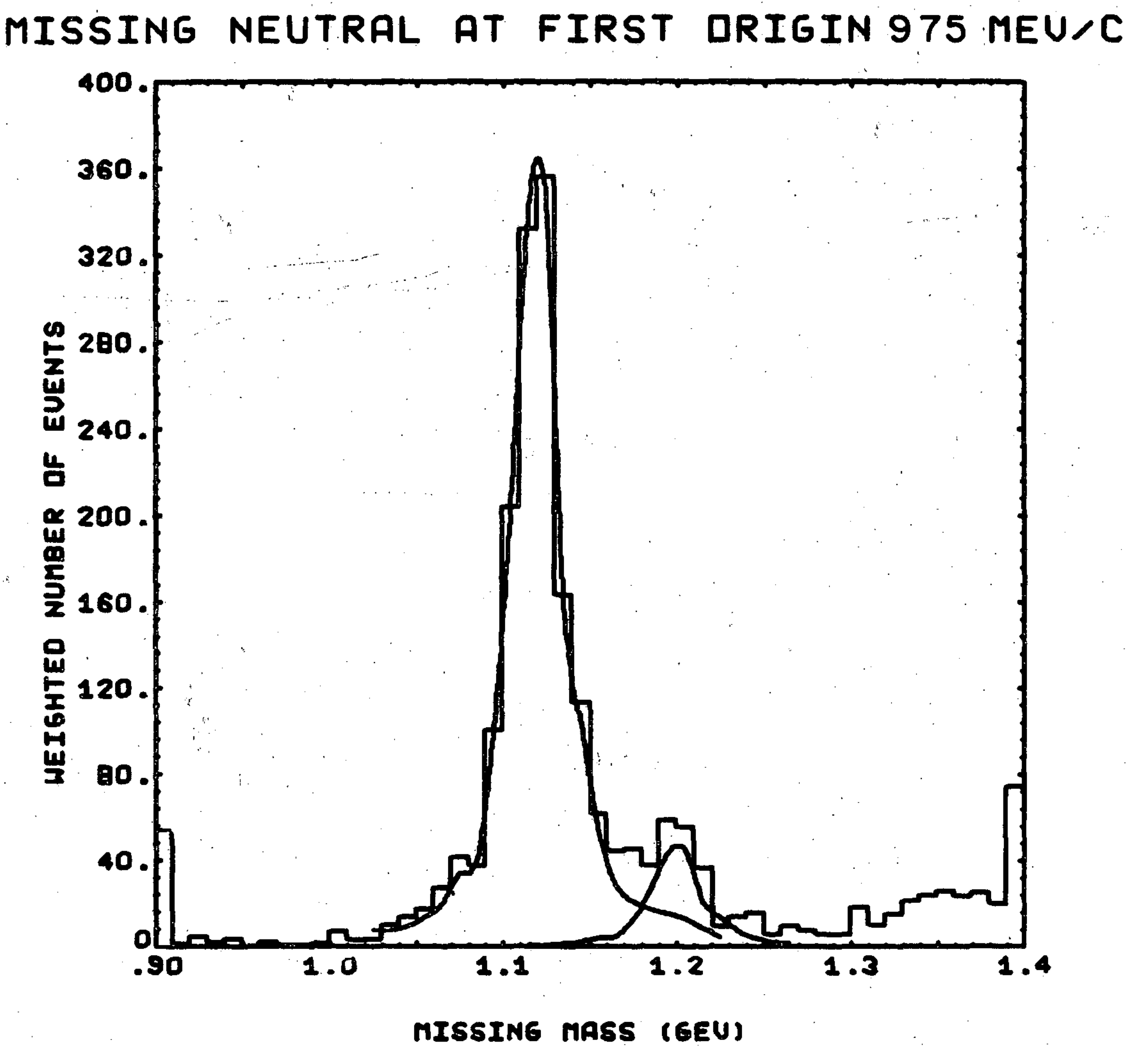

XBL 6811-6147

Fig. 3

because of the small ratio of the cross-sections for the first compared to the second reactions in our energy region; we estimate this ratio to be ~10%.

With the selection criteria described here, 19 of the events selected also constrained to the hypothesis $K^-p \rightarrow \Lambda\, \pi^+\pi^-\pi^o$.

2. Fiducial Volume and Weighting

We require the beam track to pass through the chamber thin window (rectangular area normal to beam 22 cm x 6.4 cm) and to have, before interaction, at least 3.4 cm (in space) of visible track. From chamber limitations the maximum usable beam track length for the event in this experiment is 37.4 cm.[6] The vertex of the lambda must lie inside a cylindrical volume 21.5 cm base radius by 15 cm high; the axis of this cylinder is 24.0 cm away from the up stream visible end of the chamber. This choice allows Λ decay-particles to have at least 6 cm of visible track to allow momentum measurement.

To eliminate problems arising from having the first and second vertices too close together (scanning and constraining problems), any event for which the distance between the production origin and lambda decay vertex was less than 0.8 cm in space was rejected. This condition was required on the basis of a study of the distribution of this distance.

To account for events removed by fiducial volume cuts on the second origin, every event is weighted (inversely) by the probability that the lambda might decay inside the fiducial volume. The lambda proper lifetime used in this weighting procedure is 2.52×10^{-10} sec.[7]

3. Partial cross-section

Now we have all the information we need to calculate the partial cross-section for the reaction $K^-p \rightarrow \Lambda\, \pi^+\pi^-$. The remaining steps are the following:

a. Calculate beam attenuation due to K^- - decay using K^- proper lifetime as 1.235×10^{-8} sec.[7]

b. Calculate attenuation due to interaction using the total cross-section measurement of Cool et al.[8]

c. Make corrections for the beam contamination and the scanner efficiency and various cuts made on the data (see Section B-1).

d. The density of hydrogen (0.0608 gm/cm^3) is obtained from measurement of ranges on muons from $\pi\mu e$ decay in the 25" Bubble Chamber.[9] This density leads to a mean-free-path of 435.11 cm for the natural geometric cross-section of 62.765 m.b.

For values of the cross section see Table I and Fig. 4. Our values are in good agreement with values obtained by other experimentors.[10]

C. Biases in Selected Ensemble

1. Bias in beam track count

In order to check the accuracy of beam track count we have measured the τ-decay ($K^-\pi3$) branching ratio ($K^- \rightarrow \pi^+\pi^-\pi^-$). We have scanned 66 rolls of film for events with three charged outgoing tracks, with the same beam track criteria (templates) we used in beam track counting. Scanner efficiency in this scan was 99.3%. Scanners were also to identify events where a negatively charged track and a Dalitz pair (e^+e^-) leave the origin, 3.2% of the events were identified as such. We found 2546 τ's all of which were checked on the scan table by a graduate student. Contamination to this sample would come from other K-decays that would give rise to a charged and a neutral pion, the neutral pion, converting at the origin into e^+e^- . On the basis of published K^- branching ratios[7] we find that if 50% of the above decays would "fake" a τ then this would add up to 3.3% of the number of τ's (our scanners found 3.2%). Using the published decay life-time for K^- we find a τ branching ratio

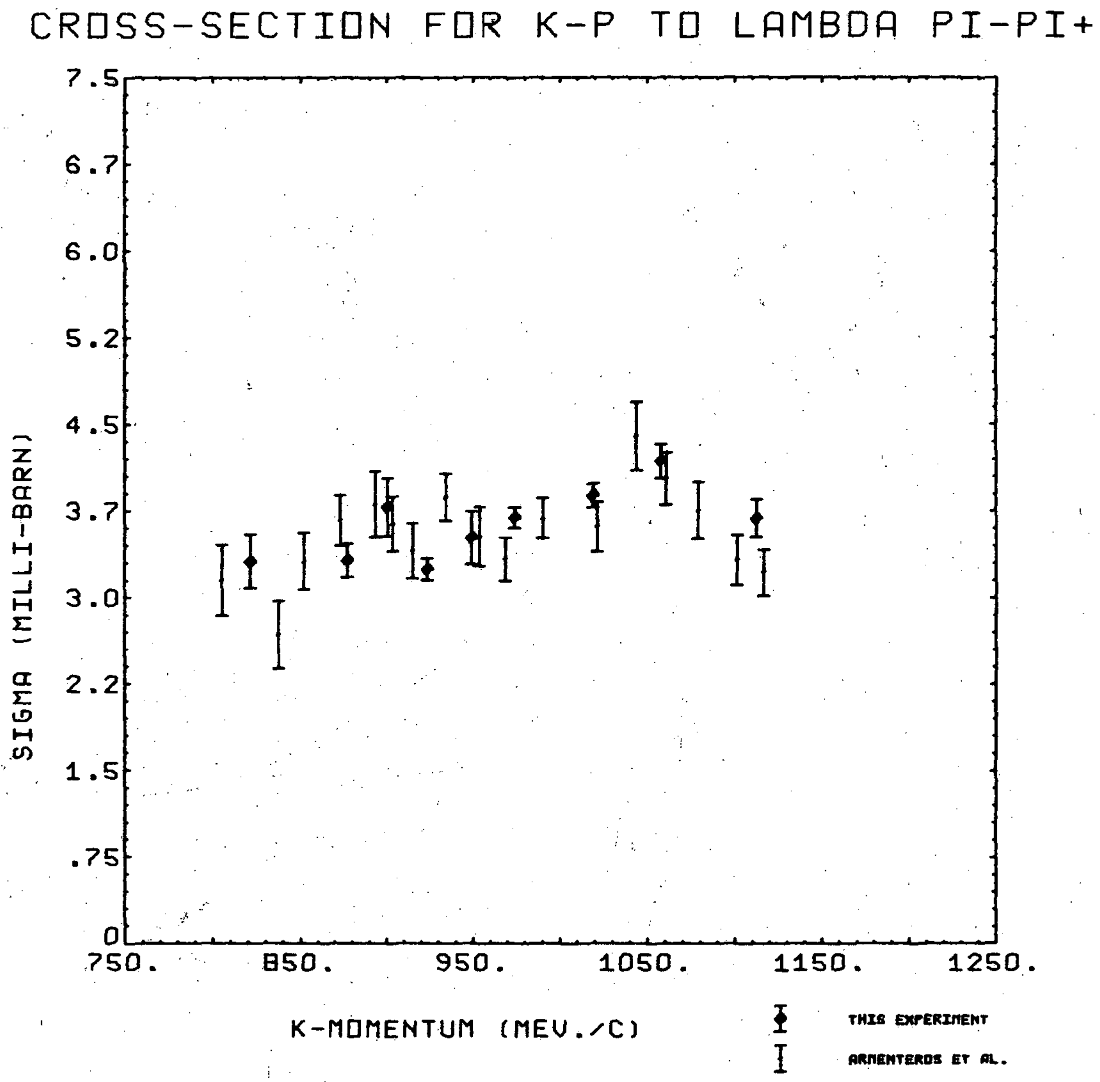

XBL 6811-6148

Fig. 4

(5.46 ± .15)% which agrees with published values.[7] Values for contamination and attenuation used here are the same as in (Section B) above.

2. Purity of lambda sample

As a test of how pure the Λ sample is, we have measured the Λ lifetime. Using Λ's which have a line of flight longer than 2 cm, and a Λ-momentum from the fitting procedure that constrains the Λ to come from the reaction origin, we find a lifetime[7a] of (2.56 ± .05) 10^{-10} sec. which is consistent with published values.[7]

3. Biases arising from chamber geometry

Fig. 5a shows the azimuthal distribution of the Λ-direction in the laboratory in the following chamber-fixed coordinate axes: Z-axis in the beam direction, X-axis in the horizontal plane. Fig. 5b shows the azimuthal distribution of the Λ decay-pion in the laboratory in the following coordinate axes: Λ-line of flight as Z-axis, X-axis in the horizontal plane. In both cases we plotted the weighted number of events as described in Section B. These histograms are flat within statistics.

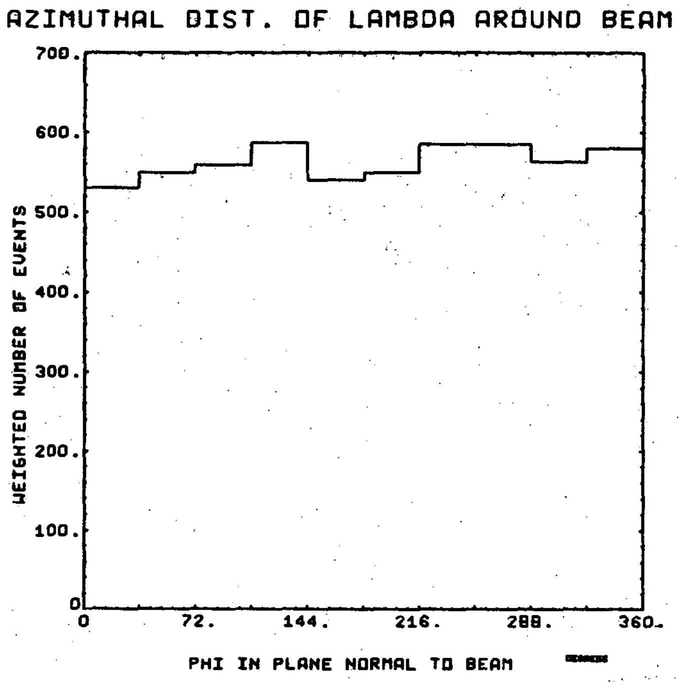

Fig. 5A

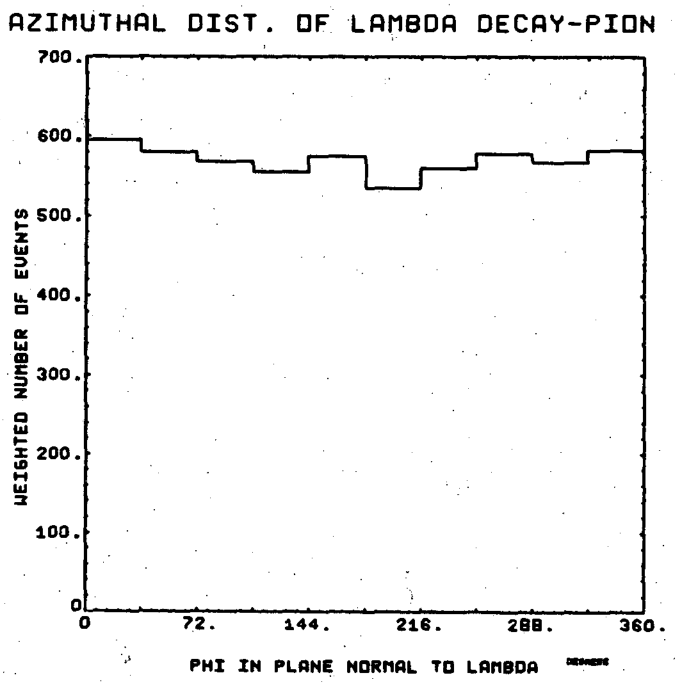

Fig. 5B

XBL 6811-6156

III. THEORETICAL FORMULATION OF THE MODEL

A. Historical Background

In the past several years there have been many attempts to develop procedures for analysis of experiments which have three particles in the final state (two spinless and one spin-1/2 particles). In 1961 Dalitz and Miller[13] discussed the effects of Bose-symmetric amplitudes in their study of the spin and parity of the $Y_1^*(1385)$. In 1963 Olsson and Yodh[14] in a model based on the work of Bergia et al.[15] developed a model for studying the N^* (3/2, 3/2) resonance, and have shown that interference terms between the iso-spin states 1/2 and 3/2 could account for the shape of the mass spectra and for the measured ratio of π^+, π^o production in the reaction $\pi^+ p \rightarrow \pi^+ p\, \pi^o$ and $\pi^+ p \rightarrow \pi^+ n\, \pi^+$.

Recently Deler and Valladas[16] have developed a practical formalism for the analysis of experiments with two spinless and one spin-1/2 particles in the final state, and in which only 2-particle interactions occur. We find this development most suited for the analysis of the present experiment and we shall describe it briefly below (Section B).

While the above formalisms bear a striking similarity to partial wave analysis for the two-body final state case, there are other methods which use weighted averages of functions of kinematical variables to determine the spin and parity of a formation resonance which decays to a less massive resonance and a boson and eventually to a 3-particle final state.[17,18,19] Whereas these methods may be powerful[20] in cases where the formation resonance dominates and does not suffer greatly from interferences with other processes, they are not suited for interactions where many angular momentum states are present, and the interference effects are not negligible.

B. Partial-Wave Analysis for a Three-Particle Final State

The reaction under consideration ($K^- p \to \Lambda \pi^+ \pi^-$) has two iso-spin states (0) and (1) present. In each of these iso-spin states the following two processes participate:[22]

a) $K^- p \to (\Lambda\pi^+)\, \pi^- \to \Lambda \pi^+ \pi^-$ $\quad Y^{*+}$ production

b) $\quad\to (\Lambda\pi^-)\, \pi^+ \to \Lambda \pi^+ \pi^-$ $\quad Y^{*-}$ production

The subsystem in parenthesis ($\Lambda\pi^{\pm}$) signifies production of an intermediate state $Y^{*\pm}$. The complete amplitude for the reaction is a coherent sum of the above, symmetrized under exchange of π^+ and π^- (Bose symmetry).

The amplitude can be written in terms of the quantum numbers of the initial, intermediate and final states and the corresponding unknown T-matrix elements, in a form similar to a partial wave expansion. Each partial wave is parameterized by two letters and a number: L the initial orbital state, L′ the orbital state betwen the subsystem ($\Lambda\pi^+$) or ($\Lambda\pi^-$) and the spectator pion and twice the total angular momentum; e.g. DS3, FP5. The amplitudes for the processes a and b must be added coherently because the two processes are indistinguishable. Thus the expressions for angular distributions and Dalitz plot densities (see Section C below, and Part IV) will show not only the familiar interference effects between the different partial waves, but also interferences between the Y^{*+} and Y^{*-} amplitudes and between the iso-spin 0 and 1 amplitudes.

A convenient choice of coordinate axes[21] in the 3-particle center of mass system (3c.m. from here on) is to take the normal to the 3-particle plane as a Z-axis and choose as X-axis the bisector of the angle between the momenta of Y^{*+} and Y^{*-}; thus the two pions are treated symmetrically. We shall refer to this system of axes as $\xi\eta\zeta$-axes Fig. 6. It is well known that we need five variables to describe three particles. We choose these to be two energies and three angles. The two energies are

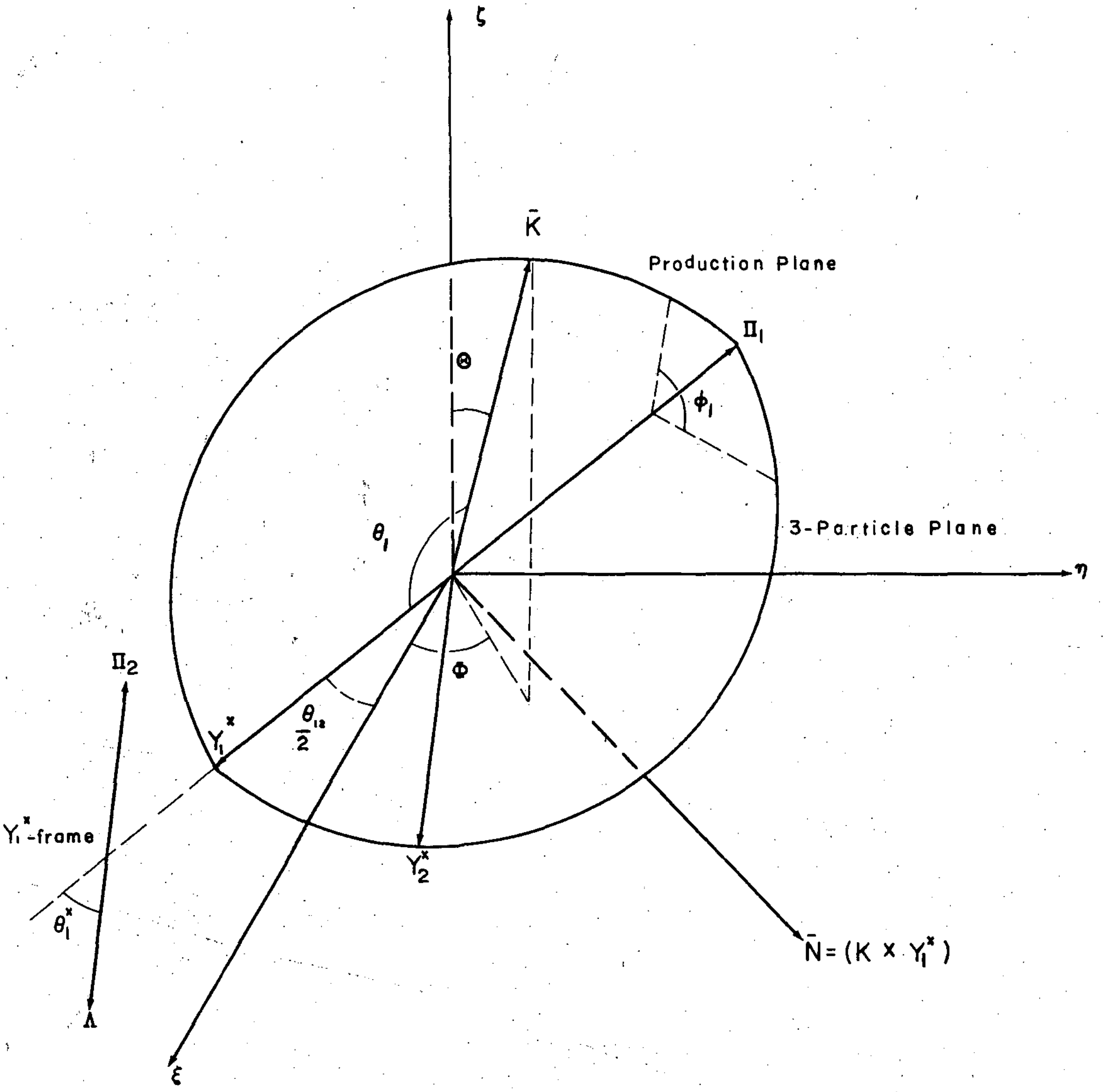

XBL 6811-6163

Fig. 6

the center of mass energies of ($\Lambda\pi^+ = Y^{*+}$) and ($\Lambda\pi^- = Y^{*-}$), whose domain of variation defines a Dalitz plot. The three angles are chosen to completely define the orientation of the above coordinate axes with respect to a fixed reference frame. If this fixed reference frame has it Z-axis along the incident direction of the K^-, then one of the three angles above is a rotation around the incident direction and is irrelevant if we have a non-polarized target; the other two are the polar angles of the incident direction in the $\xi\eta\zeta$ coordinate system defined above.

Consider one iso-spin state and the reaction $K^-p \rightarrow (\Lambda\pi_2) + \pi_1$, where only one subsystem ($\Lambda\pi_2$) is considered as an intermediate state Y^*. Let

$\vec{q}_i$ = relative momentum of K-p in 3 c.m.; $\vec{q}_i$ is along the Z-axis of a fixed reference frame.

W = total energy in 3 c.m.

J, M, L = total angular momentum, its third component, and orbital angular momentum in the initial state.

M_i = projection of proton spin along incident direction.

M_f^* = projection of Λ spin along the line of flight of ($\Lambda\pi_2$) subsystem (in 3 c.m.) as seen in the ($\Lambda\pi_2$) rest frame.

$w_1, \bar{q}_1$ = invariant mass and momentum of ($\Lambda\pi_2$) subsystem in 3 c.m.

j, λ = spin and helicity (projection of spin along line of flight) of ($\Lambda\pi_2$) subsystem in 3 c.m.

ℓ, ν = orbital angular momentum and its third component between Λ and π_2 after break-up of ($\Lambda\pi_2$) subsystem.

L' = relative angular momentum of ($\Lambda\pi_2$) and π_1.

$T_{j\ell}^{JLL'}$ = invariant reduced matrix element connecting the initial eigenstate $|WJLM\rangle$ to final eigenstate $|WJL'M; j\ell w_1\rangle$

$\bar{q}^*_1, \theta^*_1, \varphi^*_1$ = momentum and polar angles of Λ in the $(\Lambda\pi_2)$ rest frame, $(\Lambda\pi_2)$ line of flight in 3 c.m. as Z-axis and the X-axis in the production plane.

Θ, Φ = polar coordinates of incoming direction in $\xi\eta\zeta$ frame.

μ_i, μ_f = initial spin of the proton and final spin of the lambda projected on ζ -axis.

θ_{12} = angle between the direction of the two subsystems (angle between the two pions) in 3 c.m.

θ_1 = production polar angle of $(\Lambda\pi_2)$ subsystem with K^- in 3 c.m.

φ_1 = angle between normals of the 3 particle plane in 3 c.m. and the production plane of $(\Lambda\pi_2)$

Let us temporarily ignore the irrelevant rotation around the incoming direction, consider only one iso-spin state, and one combination of initial and final spin third components $\mu_i\mu_f$. Then we can write the transition between initial and final states as: (See Appendix B)

$$<(\Lambda\pi_2)\ \pi_1\ |T|\ K^-p> = \frac{1}{2\pi} \sum_{JLL'j\ell} \sqrt{\frac{2J+1}{2}}\ \frac{4W}{\sqrt{q_i}} \sqrt{\frac{4w_1}{q_1 q_1^*}}\ T^{JLL'}_{j\ell}(W, w_1)\ . \qquad (1)$$

$$f^{JLL'j\ell}_{\mu_i\mu_f}\left(\theta^*_1, \frac{\theta_{12}}{2}\right)$$

where

$$f^{JLL'j\ell}_{\mu_i\mu_f}\left(\theta^*_1, \frac{\theta_{12}}{2}\right) = \sqrt{\frac{2J+1}{2L+1}} \sum_{\lambda>0} \sum_{M^*_f} \sum_{K\ m} (-1)^{j+1/2}\ C^{JjL'}_{-\lambda\lambda 0}\ \left[1+(-1)^{L+m+1}\right]$$

$$C^{\ell\ 1/2\ j}_{\nu\ M^*_f\ \lambda}\ C^{1/2\ J\ K}_{M^*_f\ -\lambda-\nu}\ C^{1/2\ J\ K}_{\mu_f\ m-\mu_f m}\ d^K_{m,-\nu}\left(\frac{\pi}{2}\right) P^{\ell}_{\nu}(\theta^*_1)\ (-i)^{\nu}$$

$$C^{J\ 1/2\ L}_{m-\mu_f\ \mu_i\ m+\mu_i-\mu_f}\ Y^L_{m+\mu_i-\mu_f}(\Theta, \Phi)\ \exp\left(i\ m\ \frac{\theta_{12}}{2}\right)$$

The symbols $C^{\cdots}_{\cdots}$ stand for the well-known Clebsh-Gordan coefficients.

At the production origin in this experiment the processes (a) and (b) in the beginning of this section are indistinguishable. Thus to the amplitude we have written above for (a) we must add coherently the amplitude for (b). By inspecting the procedure we followed in Appendix B, it is relatively simple to find the amplitude for (b).[16] We find

$$<(\Lambda\pi_1)\,\pi_2\,|T|\,K^-p>_{\mu_i\mu_f} = \frac{1}{2\pi}\sum_{JLL'j\ell}\sqrt{\frac{2J+1}{2}}\,\frac{4W}{\sqrt{q_i}}\sqrt{\frac{4w_2}{q_2q_2^*}}\;T^{JLL'}_{j\ell}(W,w_2). \qquad (2)$$

$$f^{JLL'j\ell}_{\mu_i\mu_f}\left(-\theta_2^*,\,-\frac{\theta_{12}}{2}\right)$$

The variables with subscript 2 are defined in the same way with respect to $(\Lambda\pi_1)$ subsystem as the variables with subscript 1 related to the $(\Lambda\pi_2)$ subsystem.

$f^{JLL'j\ell}_{\mu_i\mu_f}\left(-\theta_2^*,\,-\frac{\theta_{12}}{2}\right)$ is obtained from the expression for $f^{JLL'j\ell}_{\mu_i\mu_f}\left(\theta_1^*,\,\frac{\theta_{12}}{2}\right)$ by replacing (θ_1^*) by $(-\theta_2^*)$ and (θ_{12}) by $(-\theta_{12})$.

In the reaction under study we have two iso-spin channels I_0, I_1. We can write symbolically using the relevant values of Clebsh-Gordon coefficients:

$$<\text{Amplitude}> = \sqrt{\frac{1}{2}}\left\{\sqrt{\frac{1}{3}}\,(Y^{*+},\pi^-)+\sqrt{\frac{1}{2}}\,(Y^{*-},\pi^+)\right\}<I_0> + \sqrt{\frac{1}{2}}\left\{\sqrt{\frac{1}{2}}\,(Y^{*+},\pi^-)-\sqrt{\frac{1}{2}}\,(Y^{*-},\pi^+)\right\}<I_1>$$

where we let (Y^{*+},π^-) represent the amplitude to the final state $(\Lambda\pi_2) + \pi_1$, and (Y^{*-},π^+) the amplitude to $(\Lambda\pi_1) + \pi_2$. With this we can write the complete amplitude for $K^-p \rightarrow Y_1^{*\pm}\,\pi^{\mp} \rightarrow \Lambda\pi\pi$ where Y^* has iso-spin i=1, j=3/2 and decays via p-wave (ℓ=1):

$$\langle\Lambda\pi^{+}\pi^{-}|T|K^{-}p\rangle = \frac{1}{4\pi}\sum_{\mu_i\mu_f}\;\sum_{JLL'}\sqrt{\frac{2J+1}{2}}\;\frac{4W}{\sqrt{q_i}}\;\cdot$$

$$\Bigg[\frac{1}{\sqrt{6}}\sqrt{\frac{4w_1}{q_1q_1^{*}}}\;T_{I=0}^{JLL'3/2\;1}(W,w_1)\;f_{\mu_i\mu_f}^{JLL'3/2\;1}\left(\theta_1^{*},\frac{\theta_{12}}{2}\right)$$

$$+\frac{1}{2}\sqrt{\frac{4w_2}{q_2q_2^{*}}}\;T_{I=0}^{JLL'3/2\;1}(W,w_2)\;f_{\mu_i\mu_f}^{JLL'3/2\;1}\left(-\theta_2^{*},\frac{-\theta_{12}}{2}\right)$$

$$+\frac{1}{2}\sqrt{\frac{4w_1}{q_1q_1^{*}}}\;T_{I=1}^{JLL'3/2\;1}(W,w_1)\;f_{\mu_i\mu_f}^{JLL'3/2\;1}\left(\theta_1^{*},\frac{\theta_{12}}{2}\right)$$

$$-\frac{1}{2}\sqrt{\frac{4w_2}{q_2q_2^{*}}}\;T_{I=1}^{JLL'3/2\;1}(W,w_2)\;f_{\mu_i\mu_f}^{JLL'3/2\;1}\left(-\theta_2^{*},\frac{-\theta_{12}}{2}\right)\Bigg]$$

which is a partial wave expansion in the variables $T_{I=0}$, $I_{I=1}$, and the parameters $LL'J$.

By inspection, this amplitude is found to be symmetric under exchange of the two pions since it is independent of the vector $(\bar{\pi}_1 \times \bar{\pi}_2)$ which was used to define ζ -axis.

The parameters T can be simplified by factoring out the dependence on w_1 or w_2 as a Breit-Wigner or similar form. We have followed Reference (16) and set:

$$T_{I}^{JLL'}(W,w_{1,2}) = T_{I}^{JLL'}(W)\;\frac{\sqrt{\Gamma}}{(w_{1,2}-w_r)+i\,\Gamma}\,v_{L'}$$

and used an energy dependent width (see Appendix C)

$$\Gamma = \frac{a_1\eta^3}{1+a_2\,\eta^2}$$

where η is momentum divided by mass of the decay pion $\pi_{1,2}$ in $(\Lambda\pi_{1,2})$ rest frame, a_1=0.0143 BeV, a_2=0.6395.

ψ_L, is a centrifugal barrier factor that depends on the orbital angular momentum state between the $(\Lambda\pi_{1,2})$ subsystem and the spectator pion $\pi_{2,1}$ (see Appendix C).

C. Mass - and Angular - Distributions

With the amplitude described in Section (B) we can write down the expression for the angular distribution and mass distribution. Representing this amplitude by $A_{\mu_i\mu_f}$ we have

$$d\sigma = \frac{1}{8Wq_i} \sum_{\mu_i\mu_f} \int d\alpha \;\; |A_{\mu_i\mu_f}|^2 \;\; \frac{d^3q_1}{2E_1} \; \frac{d^3q_2}{2E_2} \; \frac{d^3q_3}{2E_3} \, \delta^4 \, (Q_i - Q_f)$$

where the integration over α takes care of rotation around the incoming direction which was ignored proviously, and E_j and q_j $(j=1,3)$ are the energies and momenta of particles 1-3 in the final state. Performing change of variable and integrating over the azimuthal angle Φ we get (integration over α gives a factor 2π)

$$\frac{d\sigma}{dw_1^2 \; dw_2^2 \; d(\cos\Theta)} = \frac{(2\pi)^2}{16.16 \; q_i \; W^3} \sum_{\mu_i\mu_f} \int_{\Phi} |A_{\mu_i\mu_f}|^2 \; d\Phi$$

$A_{\mu_i\mu_f}$ contains two complex unknown parameters for each partial wave. We will use the data to fit for these.

In the above, if the values for masses and energies are in BeV then to get the cross-section in millibarn we multiply $(d\sigma)$ by the factor 0.38935 $(\text{BeV})^2$ m.b.

IV. EXPERIMENTAL APPLICATION OF THE MODEL

A. Properties of Angular Distributions from the Model

Using the model we have described in Chapter III, we have written a computer program to calculate angular distributions and Dalitz plot densities showing explicitly the dependence on the unknown parameters $T_{0,1}^{JLL'j\ell}$. The intermediate state subsystems $(\Lambda\pi_1)$, $(\Lambda\pi_2)$ are taken as $Y_1^{*-,+}(1385)$ see Section E below. To describe this procedure let us write symbolically (Chapter III, B,C)

$$\frac{d\sigma}{dw_1^2 dw_2^2 d(\cos\Theta)} \approx \sum_{\mu_i\mu_f} \int_{\Phi} |A_{\mu_i\mu_f}|^2 \, d\Phi$$

$$A_{\mu_i\mu_f} = \sum_P \Big[T_0^P(W) \left\{ F_0{}^P_{\mu_i\mu_f}(+) + F_0{}^P_{\mu_i\mu_f}(-) \right\}$$

$$+ T_1^P(W) \left\{ F_1{}^P_{\mu_i\mu_f}(+) - F_1{}^P_{\mu_i\mu_f}(-) \right\} \Big]$$

where the superscript index P represents the quantum numbers (JLL′3/2 1), the arguments (+), (-) refer to Y^{*+} and Y^{*-} production respectively. Thus referring to Chapter III, B and C, we see that

$$F_0{}^P_{\mu_i\mu_f}(+) = (\text{kinematic factors})\; v_{L'} \; \frac{\sqrt{\Gamma}}{(w_1 - w_r) + i\Gamma} \, f_{\mu_i\mu_f}^{JLL'3/2\,1}(\theta_1^*, \frac{\theta_{12}}{2})$$

The subscripts (0,1) of F refer to iso-spin states; all other indices being equal, F_0 and F_1 differ only by Clebsh-Gordan coefficients. The parameter w_r refers to the mass of the $Y_1^*(1385)$. The subscripts $\mu_i\mu_f$ which refer to initial and final spin projections will be omitted for simplicity in future reference to F.

A computer program is used to calculate the contributions to the angular distribution $d\sigma/d\,(\cos\Theta)$ which correspond to the following combinations of the unknown parameters:

a) Rl $(T_S^{*P_1}\, T_Q^{P_2})$ $S = 0,1$; $Q = 0,1$

b) Im $(T_S^{*P_1}\, T_Q^{P_2})$

where P_1, P_2 run over all the angular momentum states (JLL′), giving contributions from pure waves and interference terms between different waves. In general not all of the above eight contributions are independent. When $P_1 \equiv P_2$ and $S = Q$ then the contribution of the second combination above is zero.

The differential cross-section can then be written as

$$\frac{d\sigma}{d\Omega} \approx \sum_{P_1 \leq P_2} \sum_{S \leq Q} T_S^{*P_1}\, T_Q^{P_2}\, A_{S\ Q}^{P_1\ P_2}$$

where the $\leq$ in the first sum implies ordering only; for fixed values of P_1 and P_2 there are eight contributions to the cross-section i.e. eight functions of kinematical variables corresponding to $A_{S\ Q}^{P_1\ P_2}$, which can be calculated.

The angular distribution corresponding to each of the above combinations receives a contribution from terms of the form $F_1^{*P_1}(+)F_1^{P_2}(-)$ or $F_1^{*P_1}(+)\, F_0^{P_2}(-)$. These terms are the interference between Y^{*+} and Y^{*-} production; thus we shall call these and similar terms Bose-terms because they stem directly from the symmetry of the complete amplitude under exchange of π^- and π^+ (Chapter III-B).

The complete amplitude written in Chapter III, Section B, contains spherical harmonics $Y_m^L(\Theta,\Phi)$ with $(L + m + 1) =$ even, (see expression for $f(\theta^*, \frac{\theta_{12}}{2})$ in Chapter III). Thus the differential cross-section will contain spherical harmonics which have $(L + m)$ even. To see this remember the addition theorem for spherical harmonics:

$$Y^{\ell_1}_{m_1}(\theta,\varphi)Y^{\ell_2}_{m_2}(\theta,\varphi)=\sum_{|\ell_1-\ell_2|\leq\ell_3\leq\ell_1+\ell_2}\sqrt{\frac{(2\ell_1+1)(2\ell_2+1)}{4\pi(2\ell_3+1)}}\,C^{\ell_1\ell_2\ell_3}_{0\;0\;0}\,C^{\ell_1\ell_2\ell_3}_{m_1m_2m_3}\,Y^{\ell_3}_{m_3}(\theta,\varphi)$$

$C^{\ell_1\ell_2\ell_3}_{0\;0\;0}$ is the parity coefficient which is zero unless $\ell_1 + \ell_2 + \ell_3 =$ even. We remember that Θ, Φ are polar coordinates of the incoming direction in the $\xi\eta\zeta$ coordinate axes in 3-c.m., ζ is normal to the 3-particle plane and $(-\xi)$ is the bisector of $\pi_1\pi_2$ angle. From the symmetry property above, the angular distributions in Θ after integration over Φ are symmetric with respect to $\cos\Theta = 0$ and thus do not receive any contribution from interferences of odd-relative-parity waves (e.g. DS3 and PP3; or DD5 and FP5). However we can express these angular distributions in terms of the production angles of Y^{*+}, Y^{*-} ($\cos\theta_1=\vec{K}\cdot\vec{Y}^{*+}$, $\cos\theta_2=\vec{K}\cdot\vec{Y}^{*-}$). These angles are more familiar to experimental physicists. Therefore to be more explicit we use the general symmetric form of the amplitude and make a transformation from (Θ,Φ) to (θ_1,φ_1) in the Y^{*+} half of the Dalitz plot or to (θ_2,φ_2) in the Y^{*-} half of the Dalitz plot, where φ_1 and φ_2 are angles between the production and decay planes for Y^{*+} and Y^{*-} respectively. See Fig. 6, Chapter III. The angular distribution coefficients of the parameters in expression 1 above are expressed in terms of these angles θ_1 and θ_2. We list here some of the properties of the production angular distribution obtained in the above manner:

a) Distributions for pure waves or between waves of even relative-parity are even; those between waves of odd-relative-parity are odd with respect to $\cos\theta_{1,2} \rightarrow -\cos\theta_{1,2}$. Contributions to the differential cross-section (i.e. integrating over θ_1,θ_2) are nonzero only for pure waves and interference terms between waves of the same parity and total angular momentum (e.g. DS3 and DD3, or FP5 and FF5). These results are very well known.

b) For interference between iso-spins zero and one, the contribution to the angular distribution in the Y^{*+} region (1/2 of Dalitz plot) are of opposite sign to the contribution in the Y^{*-} region (the other 1/2 of the Dalitz plot) but they are of equal magnitudes. This effect can make the experimental production angular distributions have a different character for Y^{*+} compared to Y^{*-}. To see this we remember that the contribution to the angular distribution from the interference terms between waves of odd-relative parity are antisymmetric under $\cos\theta_{1,2} \rightarrow -\cos\theta_{1,2}$. Therefore the interference terms between the iso-spin states 0 and 1 and between waves of odd-relative parity can make the production angular distribution lopsided, one way for the Y^{*+} and the opposite way for the Y^{*-} production.

c) The centrifugal barrier introduced in Chapter III has a small effect (2-10 percent) on the shape of the angular distributions, and is not the same for all waves. The effect is largest near $\cos\theta_{1,2} = \pm 1$.

In Table II we give as an example the functional form of the angular distribution for some of the waves and their interference terms.[25] These are given for pure iso-spin state, no interference between the different charge states of Y^*, and as a function of the production angle of the Y^*.

Table II

Wave or Interference Term	Contribution to the Angular Distribution
PP3	$1.-080P_2(\cos\theta)$
PP3 DD5	$2.46P_1(\cos\theta) - 1.87P_3(\cos\theta)$
PP3 FP5	$1.20P_2(\cos\theta)$
DD5	$1. + 0.408P_2(\cos\theta) - 0.98P_4(\cos\theta)$
DD5 FP5	$0.351P_1(\cos\theta) + 1.4P_3(\cos\theta)$
FP5	$1. + 0.80P_2(\cos\theta)$

B. Properties of Mass Distributions from the Model

The Dalitz plot receives non-zero contributions from interference terms between waves of the same angular momentum and parity (e.g. DS3 and DD3, FP5 and FF5 etc.) only. We have parametrized these interference terms in the same way as for the angular distributions above.

Referring to Section (A) above we can write symbolically the Dalitz plot density for a pure wave: (deleting superscripts P)

$$\begin{aligned}\frac{\sigma d\sigma}{dw_1 dw_2} \approx\ & |T_0|^2 \left\{ |F_0(+)|^2 + |F_0(-)|^2 + 2\mathrm{Rl}\ (F_0^*(+)F_0(-)) \right\} \\ & + |T_1|^2 \left\{ |F_1(+)|^2 + |F_1(-)|^2 - 2\mathrm{Rl}\ (F_1^*(+)F_1(-)) \right\} \\ & + \mathrm{Rl}\ (T_0^* T_1) \left\{ F_0^*(+)F_1(+) - F_0^*(-)F_1(-) \right\} \\ & + \mathrm{Im}\ (T_0^* T_1)\ \mathrm{Im} \left\{ F_0^*(-)F_1(+) - F_0^*(+)F_1(-) \right\}\end{aligned}$$

We must remember that F_1 and F_0, all other indices being equal, differ only by Clebsh-Gordan coeficients; thus the third curled bracket is real and the fourth curled bracket is pure imaginary. We also see immediately that in the first and second curled brackets the interference terms are equal, up to a multiplicative factor; these two terms together with the fourth curled bracket are the Bose terms, since they are a consequence of symmetrization. These terms will vanish if the Y^* has zero width.

The Dalitz plot density for pure waves is parametrized to be the sum of four terms which are contributions of four independent combinations of the unknown parameters. These combinations are as follows:

1) $1/2\ (1/4\ |T_1|^2 + 1/6\ |T_0|^2)$

2) $1/2\ (-1/4\ |T_1|^2 + 1/6\ |T_0|^2)$

3) $1/\sqrt{6}\ \mathrm{Rl}\ (T_0^* T_1)$

4) $1/\sqrt{6}\ \mathrm{Im}\ (T_0^* T_1)$

It is interesting to note that the second combination above comes from the interference of the two Y^*'s only.

We will give some properties of the components of the Dalitz plot distributions relevant to the above parameterization.

a) Contribution of combination(1) is a distribution symmetric with respect to the line $w_1^2 = w_2^2$ (when we talk about symmetry or antisymmetry of the Dalitz plot distribution from here on, it is with respect to this line). In fact each of the 2 components of 1) has the same distribution. They also show the Y^{*+} and Y^{*-} resonance bands as expected. This contribution is always positive.

b) The contribution of term(2) above is symmetric and it has the largest absolute value in the region where the Y^* bands come closest together. This term oscillates from negative to positive, and is zero at least once in each half of the Dalitz plot.

c) Contributions from the terms (3) and (4) are always antisymmetric and do not contribute to the partial cross-section (i.e. integration of these contributions over the whole Dalitz plot yields zero). The contributions of these terms enhance the production of the Y^{*+} at the expense of the Y^{*-} or vice versa. Contributions of (3) is zero along the line $w_1^2 = w_2^2$, but (4) can be zero at other regions of the Dalitz plot also. In Fig. 7 we show a sample of contributions to the Dalitz plot from each of the four combinations above.

Property b) could be of major consequence. Its effect may be seen experimentally as an apparent shift in the position of the Y^*-peak. To see this let us pick the wave FP5 at ∼1058 MeV/c incoming momentum for the reaction $K^- p \to \Lambda \pi^+ \pi^-$. If we project the Dalitz plot density along

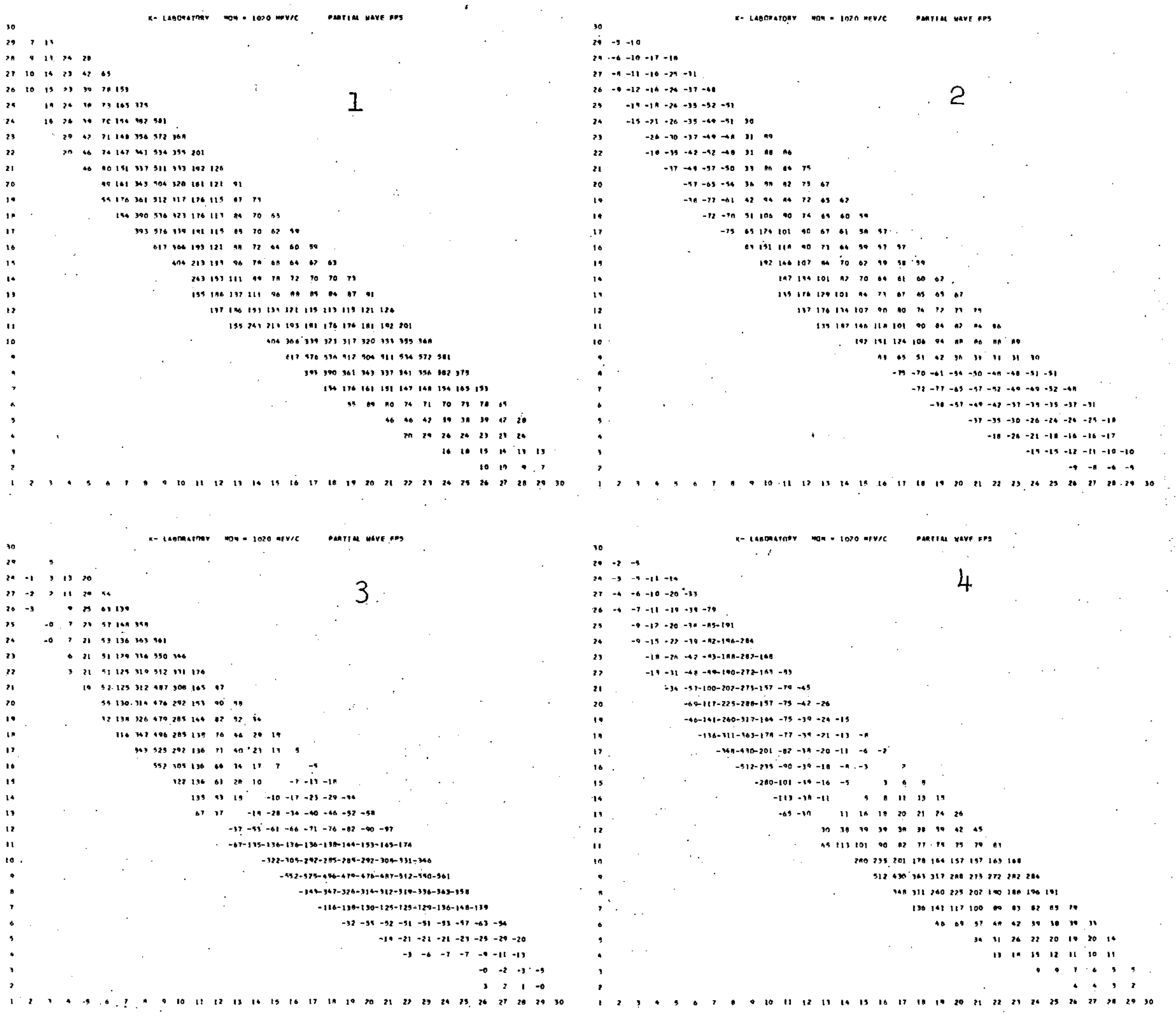

Fig. 7

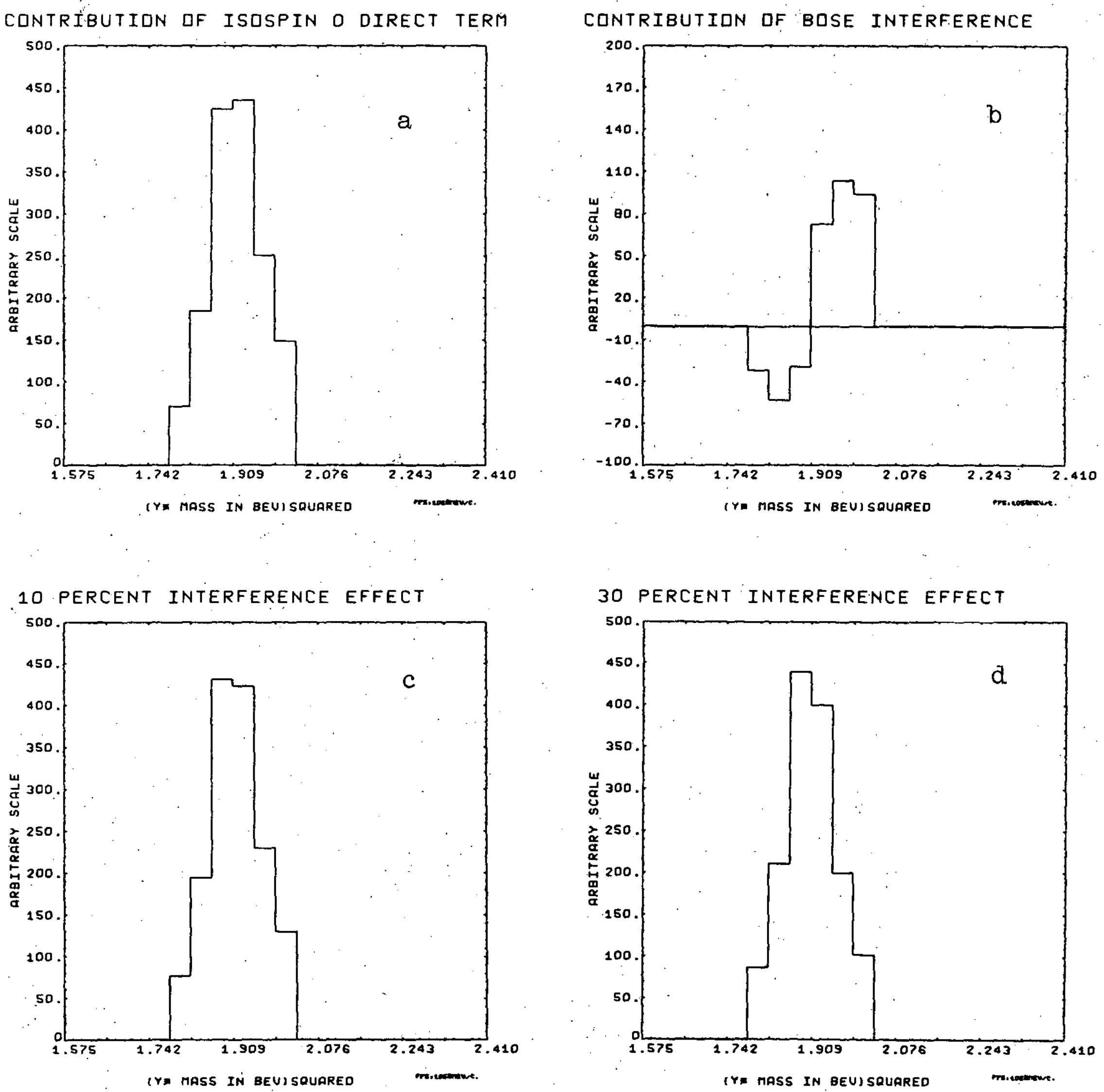

XBL 6811-6157

Fig. 8

the Y^{*+} axis for the contribution (1) and (2) separately (direct term and Bose term) and plot the region of the peak we get Fig. (8a,b); the next two histograms (8c,d) show the position of the peak when the contribution (1) and (2) are added in the ratio 10:1 (8c), and when they are added in the ratio 10:3 (8d). This shift depends on the ratio of the partial cross-section in the iso-spin state zero compared to the iso-spin state one; thus the shift in the position of the peak can be towards higher or lower mass. The experimentally measured mass-difference between Y^{*+} and Y^{*-} can not be explained by this effect because it shifts both Y^{*+} and Y^{*-} in the same direction (see Section D below).

The projection of the Dalitz plot density upon an axis parallel to the Y^{*+} (or Y^{*-}) band gives the decay distribution of the Y^{*+} (or Y^{*-}) as a function of the cosine of its decay angle in its rest frame θ_1^* (or θ_2^*). A downward concavity in the decay distribution comes from the two families of waves: $L = L' = J-1/2$ (e.g. PP3, DD5, FF7) and $L = L' = J + 1/2$ (e.g. DD3, FF5) with the exclusion of the wave PP1.[29] The experimental decay distributions are shown in Fig. 9. The lopsidedness of the experimental distributions is partly due to the interference between the different charge states of the Y^*.

C. Fitting Procedure

We have divided the data into two parts along the symmetry axis of the Dalitz plot (we shall refer to these as Y^{*+} region and Y^{*-} regions) and plotted the experimental angular distributions as a function of the production angle θ_1 of $Y^{*+}(1385)$ in the Y^{*+} region, and as function of the production angle θ_2 of Y^{*-} in the Y^{*-} region.

We set the experimental Dalitz plots on a 30 x 30 grid for each momentum, the coordinates of the plot spanning the region allowed by

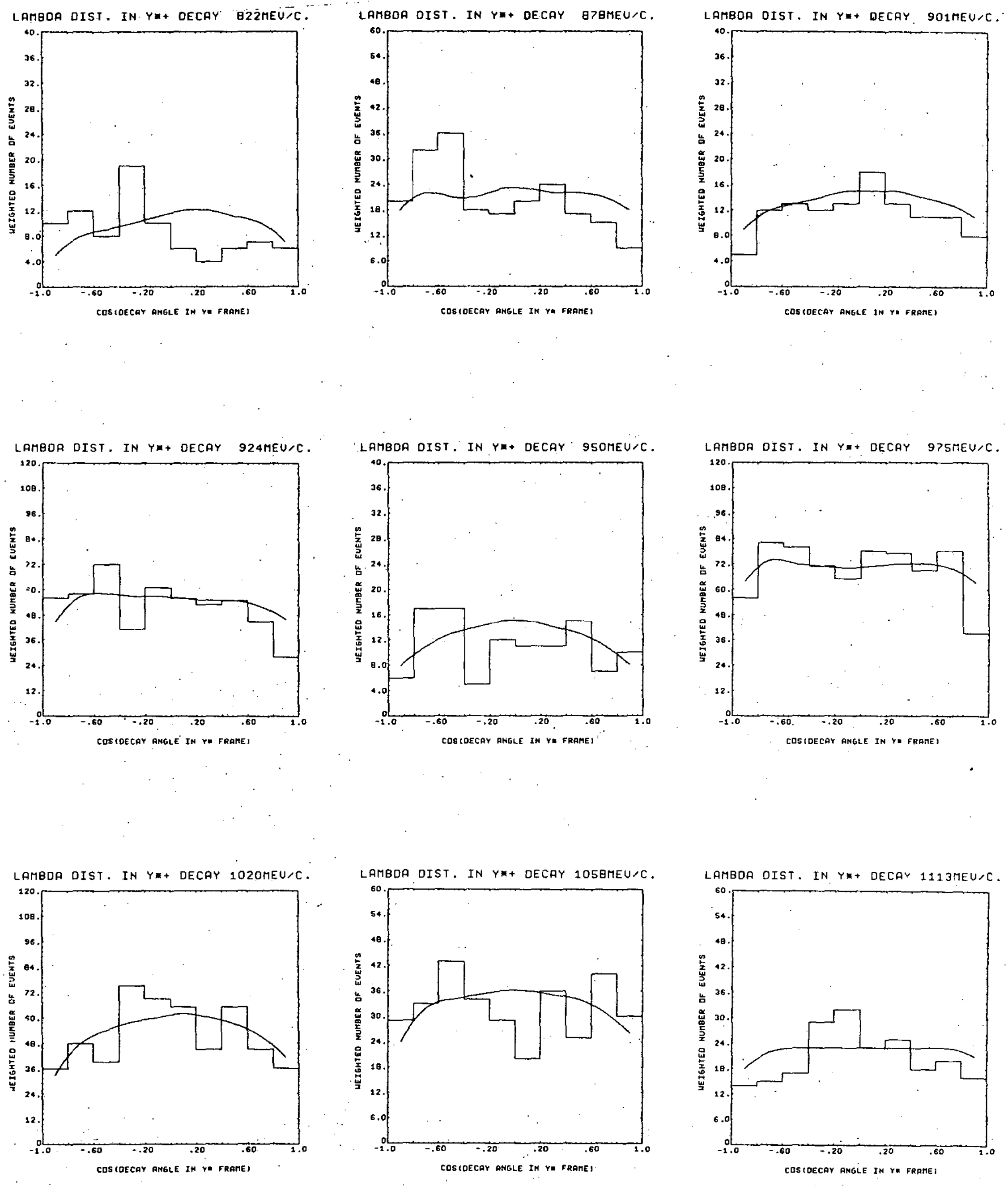

LAMBDA DIST. IN Y*+ DECAY 822MEV/C.

LAMBDA DIST. IN Y*+ DECAY 878MEV/C.

LAMBDA DIST. IN Y*+ DECAY 901MEV/C.

LAMBDA DIST. IN Y*+ DECAY 924MEV/C.

LAMBDA DIST. IN Y*+ DECAY 950MEV/C.

LAMBDA DIST. IN Y*+ DECAY 975MEV/C.

LAMBDA DIST. IN Y*+ DECAY 1020MEV/C.

LAMBDA DIST. IN Y*+ DECAY 1058MEV/C.

LAMBDA DIST. IN Y*+ DECAY 1113MEV/C.

XBL 6811-6152

Fig. 9A

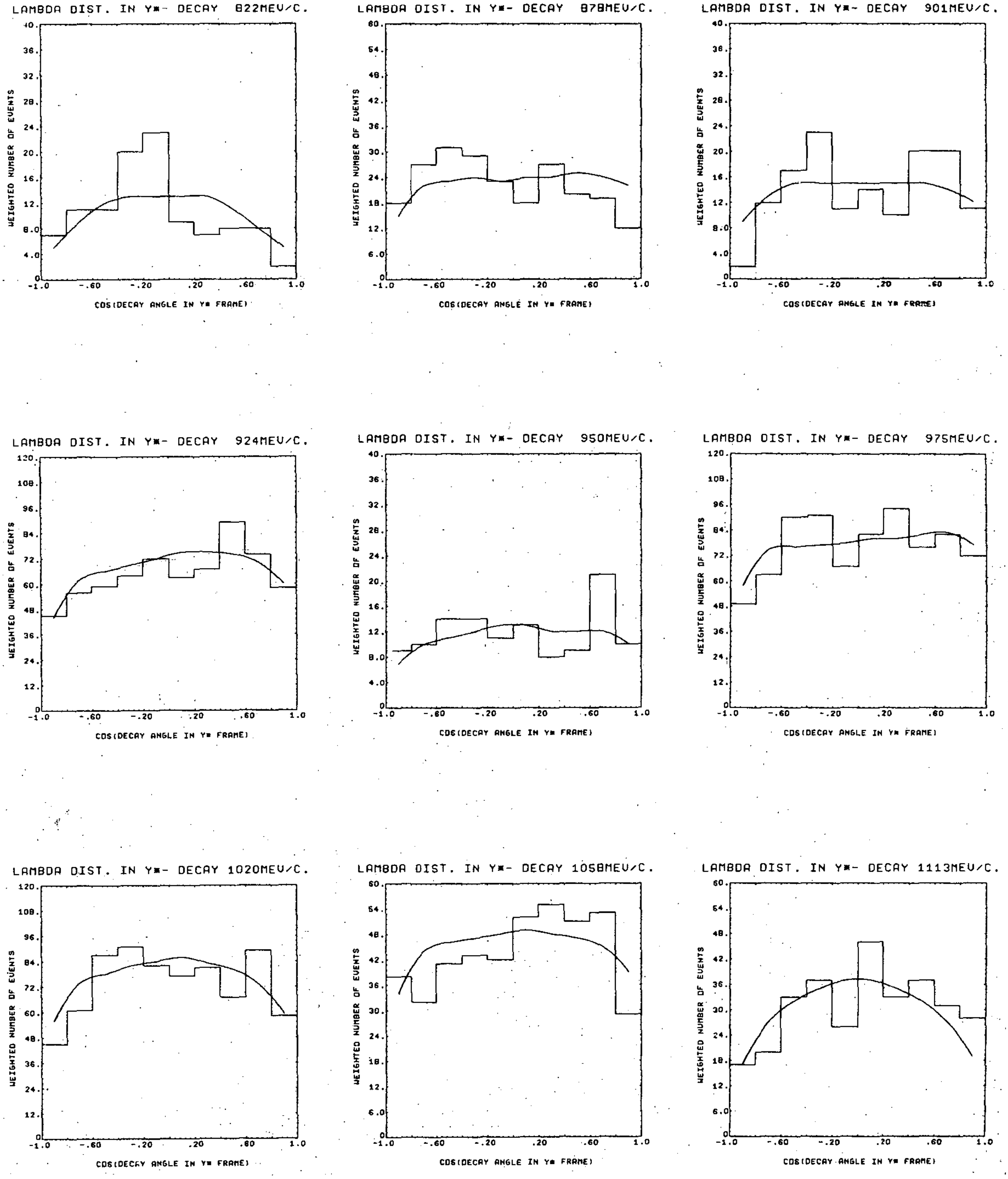

XBL 6811-6169

Fig. 9B

conservation laws. We bin the Dalitz plots by adding grid points parallel to the Y^* bands until we accumulate a statistically meaningful number of events in each bin (or, as an option, until we cover equal areas of phase space).

We bin the calculated distributions in the same way exactly. We remember that the calculated distributions consist of eight contributions for each wave and interference term for the angular distributions; for the Dalitz plot density, they consist of four terms for pure waves and eight contributions for interference terms.

The fitting is done in the following manner

a) With a certain hypothesis for the values of the complex parameters T_1 and T_0 for each partial wave we build an angular distribution and Dalitz plot density binned exactly in the same manner as the data.

b) Construct a χ^2 function for the goodness of fit of the theoretical distribution to the experimental distribution. This is done jointly for the angular distribution and Dalitz plot.

c) Vary the values of the parameters systematically to arrive at a minimum in χ^2. For this we have used a variable metric minimization program.[26]

d) The values of the parameters from the fit are normalized to give a partial cross-section equal to the experimentally measured one.

We have used the partial waves: PP1, DS3, PP3, DD3, DD5, FP5, and FF5. We do not go beyond angular momenta of 5/2 since the FF7, if present, will have a very small contribution at our energies because of centrifugal barrier effects (see below); and the GD7 waves, if present, will be negligibly small at momenta in this experiment.

The waves FP5 and FF5 have the same total angular momentum and the same initial orbital state, thus we assume that they have the same amplitude up to a phase and a centrifugal barrier factor. If their amplitudes are equal then their contributions to the partial cross-sections are in the ratio ~19:1. The above is also true for DS3 and DD3 giving a ratio of ~5:1. (These ratios are given for K^- incoming momentum of 1020 MeV/c).

We have ignored the waves SD1, PF3, DG5 on the basis of arguments similar to the above.

D. $Y^{*-} - Y^{*+}$ Mass Difference

Many experimentors have measured the mass difference between the different charge states of the $Y_1^*(1385)$.[7,27] Reference 27 gives

$$(Y^{*-} - Y^{*+})\text{ mass difference} = 4.3 \pm 2.2\text{ MeV.}$$

A calculation by Soclow and Coleman[28] (involving a combination of scaler meson tadpoles, an intermediate state involving a Y_1^* and a photon, and intermediate state involving one Σ and a photon), yields a mass difference $(Y^{*-} - Y^{*+})$ 8.5 to 10.8 MeV.

In our fitting procedure we have varied the masses of Y^{*+} and Y^{*-} to arrive at a best fit. This is done by varying the positions of the Y^* bands in the Dalitz plot in the data with respect to fixed plot boundary at each momentum. Ordinarily the masses are made variable in the model used to fit the data; however since the bands are moved by less than 6 MeV (~5% of the width of the Dalitz plot) we expect the difference between these two methods to be negligible.

E. Characteristics of the Dalitz Plot Distributions

In Table III we show a summary of general characteristics of the experimental Dalitz plot distribution at each momentum. The column labled (Outside Bounds) contains the number of events that lie outside the plot's kinematic boundary for the given values of the momentum; this

Table III.

Momentum of K^- MeV/c	Weighted Events Y^{*+} Region	Y^{*-} Region	Outside Bounds	Average Weight Per Event	Back-Ground %
822	95	114	16	1.280	23
878	231	239	40	1.240	21
901	125	151	19	1.244	23
924	591	710	97	1.272	22
950	120	123	12	1.233	21
975	762	833	133	1.240	20
1020	570	805	94	1.265	18
1058	349	479	61	1.265	18
1113	218	326	26	1.260	20

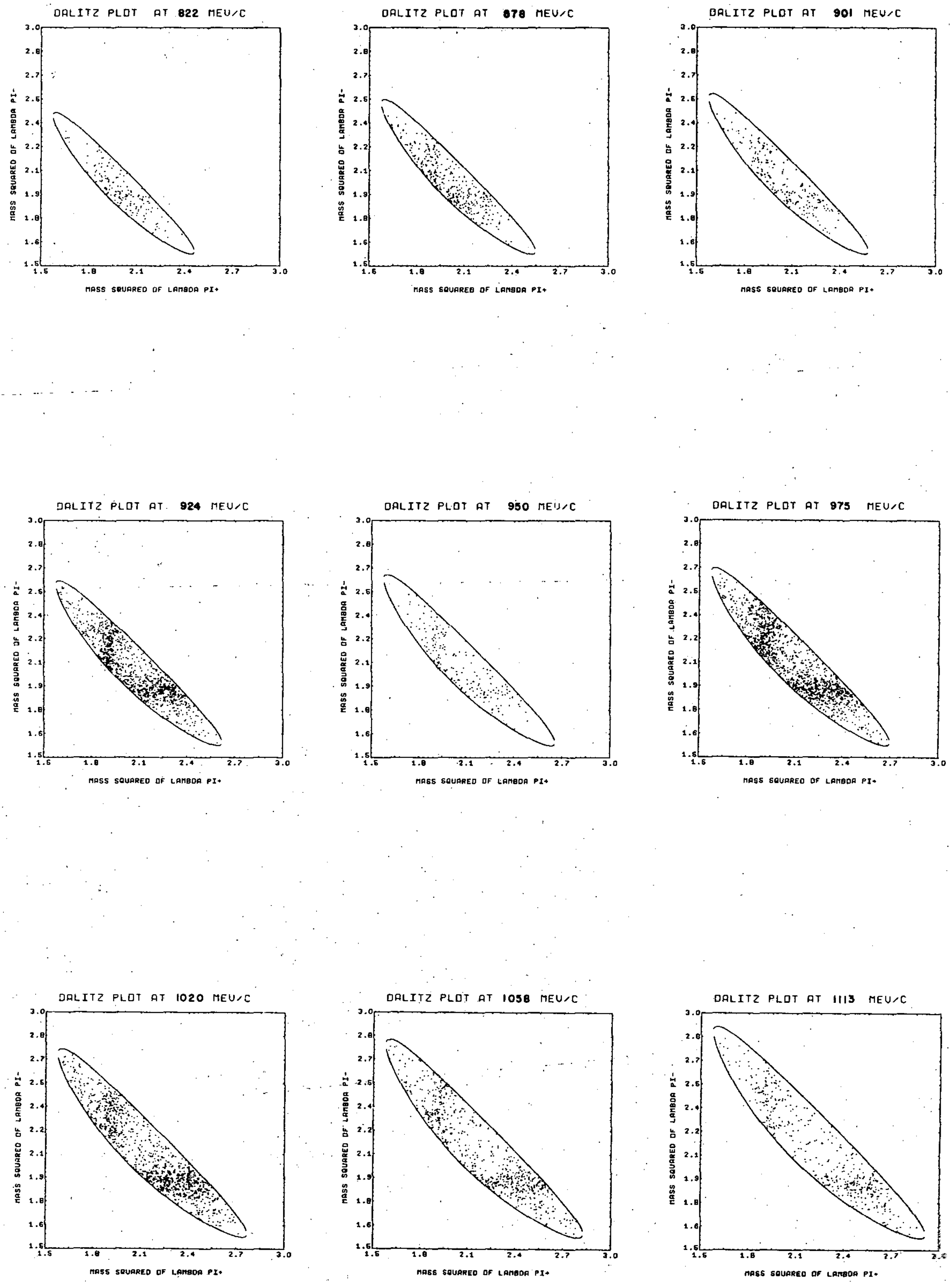

XBL 6811-6153

Fig. 10

comes mainly from the spread in the beam momentum. The background given is estimated by counting the number of events outside the Y^* bands region (i.e. a strip 114 MeV wide along each resonance band), and adjusting to the total area of three-body phase space. Fig. 10 shows the experimental Dalitz plots with the events outside the bounds removed.

The fact that the majority of the events are accounted for by $Y^*(1385)$ production (Table III) justifies the assumption made in Chapter III in choosing a model to describe the data, i.e. a model which considers only ($K^-p \rightarrow Y^{*\pm} + \pi^{\mp} \rightarrow \Lambda\ \pi^+\pi^-$). The remaining fraction of the events which we call background in Table III, are accounted for by using a 3-body s-wave non-interferring background. This adds another unknown parameter to the fitting procedure.

F. Lambda Polarization

In Chapter III the angular distributions from the model are expressed as a sum over the values of μ_f which is the component of the final Λ spin along the quantization axis (ζ). The eigenstates of spin of the lambda in the final state quantized along the production normal of the Y^* (Y^{*+} or Y^{*-} depending on the region of the Dalitz plot considered) can be obtained by a transformation of the spin state upon rotating the coordinate system $\xi\eta\zeta$ to the system XYZ; where the production normal is taken as the Z-axis, the Y-axis along the incoming direction and the X-axis in the production plane. The transformation is carried out by the operators $D^{1/2}_{mm'}(\alpha,\beta,\gamma)$[32] where the angles α,β,γ are shown in Fig. 11. The angles α and γ introduce a phase only, and $\cos\beta = \hat{Z}\cdot\hat{\zeta}$. In this manner one obtains the contributions to the (model-dependent) angular distributions from the final states which have spin-up (or spin-down) lambda spin projection along the production normal. These angular distributions can be obtained as a

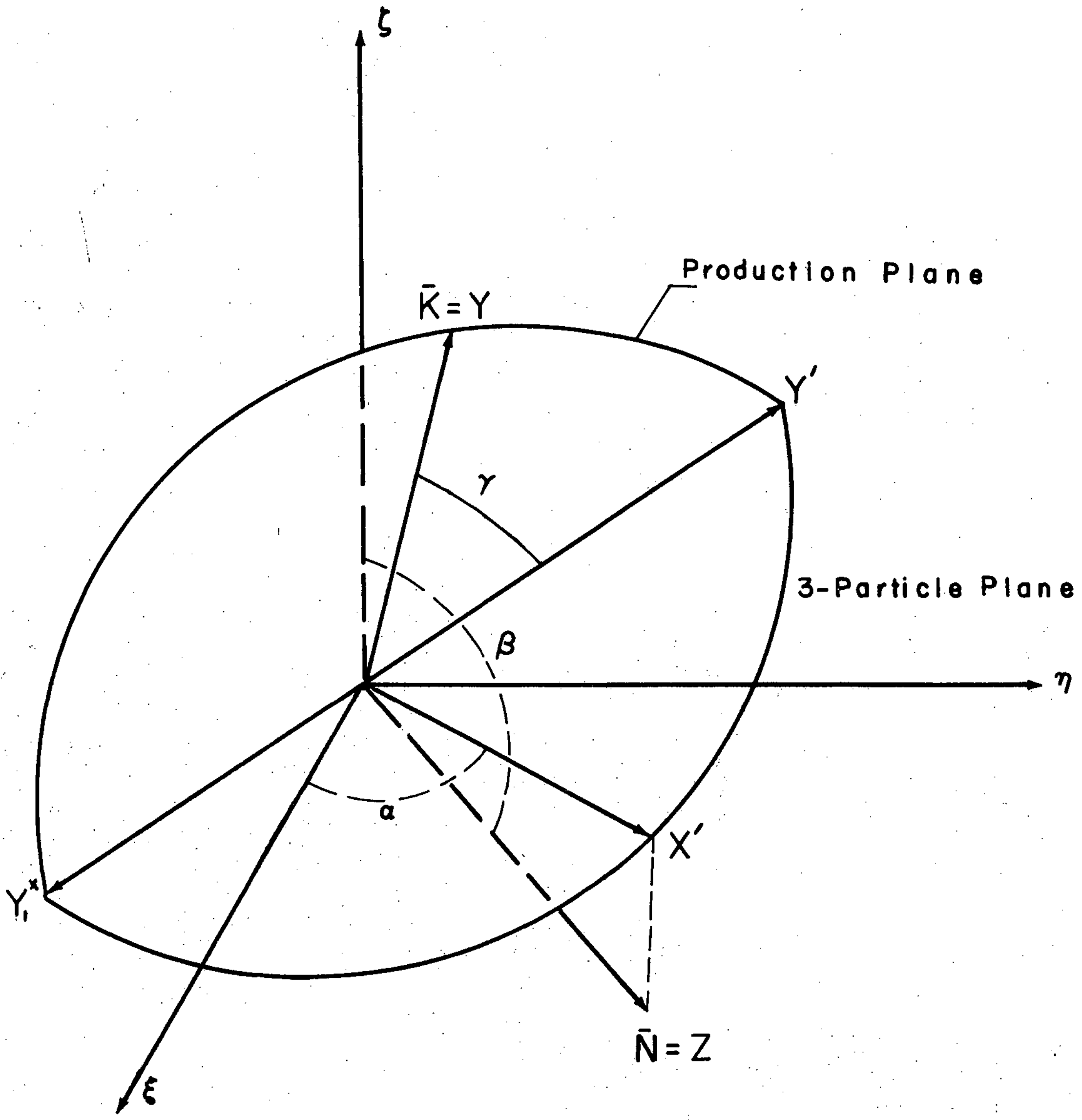

$$\alpha = (\pi - \theta_{12})/2$$

$$\mathrm{COS}(\beta) = \bar{\zeta} \cdot \bar{N}$$

$$\gamma = \pi - \mathrm{ARCCOS}(\bar{K} \cdot \bar{Y}_1^*)$$

XBL 6811-6162

Fig. 11

function of the angle between the Λ in the Y^* frame and the production normal. If $\hat{\Lambda}^*$ is a unit vector in the direction of the Λ in Y^* frame then the cosine of this angle is (symbols designating unit vectors, see Fig. 6, Chapter III)

$$\hat{\Lambda}^* \cdot Z = \sin\theta^* \sin\varphi \text{ with } \cos\theta^* = \hat{\Lambda}^* \cdot Y^*; \ \cos\varphi = \zeta \cdot Z$$

If the values of the parameters (Section A above) are known then the polarization of the lambda along the Y^* production normal can be calculated as a function of $\hat{\Lambda}^* \cdot Z$ in the usual way.

These polarization distributions are symmetric under $(\hat{\Lambda}^* \cdot \hat{Z}) \rightarrow -(\hat{\Lambda}^* \cdot \hat{Z})$. This can be seen if we remember that the angular distributions are symmetric under $\Theta \rightarrow \pi - \Theta$, $(\Theta = \hat{K}^- \cdot \hat{\zeta})$, which implies inversion of the direction of the Z-axis defined above, see Fig. 11, Chapter IV-A and Chapter III-B.

If the lambda has a polarization $(\hat{P} \cdot \hat{Z})$ along the direction $\hat{Z}$, then its decay-proton angular distribution will be

$$\frac{d\sigma}{d(\hat{P} \cdot \hat{Z})} = 1 + \alpha\,(\hat{P} \cdot \hat{Z}) \cos a \ , \ \cos a = \hat{p} \cdot \hat{Z}$$

where α is the decay asymmetry parameter of the lambda[7] = 0.646, and $(\hat{p})$ is a unit vector in the direction of the decay proton in the lambda rest frame.

Thus experimentally we have

$$< \alpha\, \hat{P} \cdot \hat{Z} > = \frac{3}{N} \sum_i^N \hat{p}_i \cdot \hat{Z} = \frac{3}{N} \sum_i^N \cos a_i$$

where the sum is over all the data, with weights taken into account; and the error on this average is:

$$\Delta\,(\alpha\, \hat{P} \cdot \hat{Z}) = \frac{1}{\sqrt{N}} \left\{ 3 - (\alpha\, \hat{P} \cdot \hat{Z})^2 \right\}^{1/2}$$

The polarization distributions as a function of $\hat{\Lambda} \cdot \hat{Z}$, where Z is the production normal, are shown in Fig. 12 and Table III-A for Y^{*+} and Y^{*-} folded with respect to $\hat{\Lambda} \cdot \hat{Z} = 0$. The unfolded distributions are symmetric within their errors. These distributions are for the range -0.8 to +0.8 in the cosine of the production angle $(\hat{Y}^{*} \cdot \hat{K})$.

This polarization information is used in fitting for the unknown parameters in the same manner as are the angular distributions. For an initial geuss of the parameters, the contributions to the angular distribution for the different spin projections of the Λ spin along the production normal are calculated, then the polarization is calculated and compared with the experimental values. The chi-square is then systematically minimized simultaneously with the chi-square for the angular distribution and the Dalitz plot density.

Table III-A. Lambda polarization as a function of the cosine of the angle between the Λ in the $Y^{*\pm}$ rest frame and the $Y^{*\pm}$ production normal for the range -.8 to +.8 in $(\bar{K}\cdot Y^{*\pm})$ folded about $(\hat{\Lambda}\cdot\hat{Z})$ = 0.

Range of $(\hat{\Lambda}\cdot\hat{N})$	Beam Momenta GeV/c .822	.878	.901	.924	.950	.975	1.020	1.058	1.113	
-1. -.8	*	.23±.38	*	.19±.24	*	.15±.20	.40±.24	.15±.37	.29±.38	Y_1^{*+}(1385) Production
-.8 -.6	.12±.48	*	.18±.35	-.15±.28	.61±.35	-.13±.23	.42±.29	-.23±.33	.30±.50	
-.6 -.4	*	- .21±.32	*	.34±.28	*	.42±.26	-.17±.32	-.51±.41	-.59±.51	
-.4 -.2	*	*	*	0.0±.31	*	.28±.31	-.41±.32	*	-.20±.52	
-.2 0.	.06±.38	.27±.35	- .46±.39	.08±.35	.36±.41	.32±.28	.12±.37	-.07±.34	-.60±.50	
-1. -.8	*	.05±.38	*	.38±.21	*	. 5±.19	.31±.20	.42±.29	.32±.31	Y_1^{*-}(1385) Production
-.8 -.6	.17±.41	*	- .04±.31	-.11±.25	.36±.38	-.07±.23	.17±.25	.34±.30	0.0±.36	
-.6 -.4	*	- .70±.28	*	.09±.27	*	-.71±.23	.23±.25	-.05±.34	.19±.45	
-.4 -.2	*	*	*	-.64±.28	*	-.43±.26	-.35±.29	.20±.33	-.24±.41	
-.2 0.	-.17±.37	-1.17±.32	-1.06±.35	-.19±.28	-.92±.35	-.45±.28	-.22±.30	-.75±.36	-.94±.41	

* indicates the lower limit of an enlarged interval.

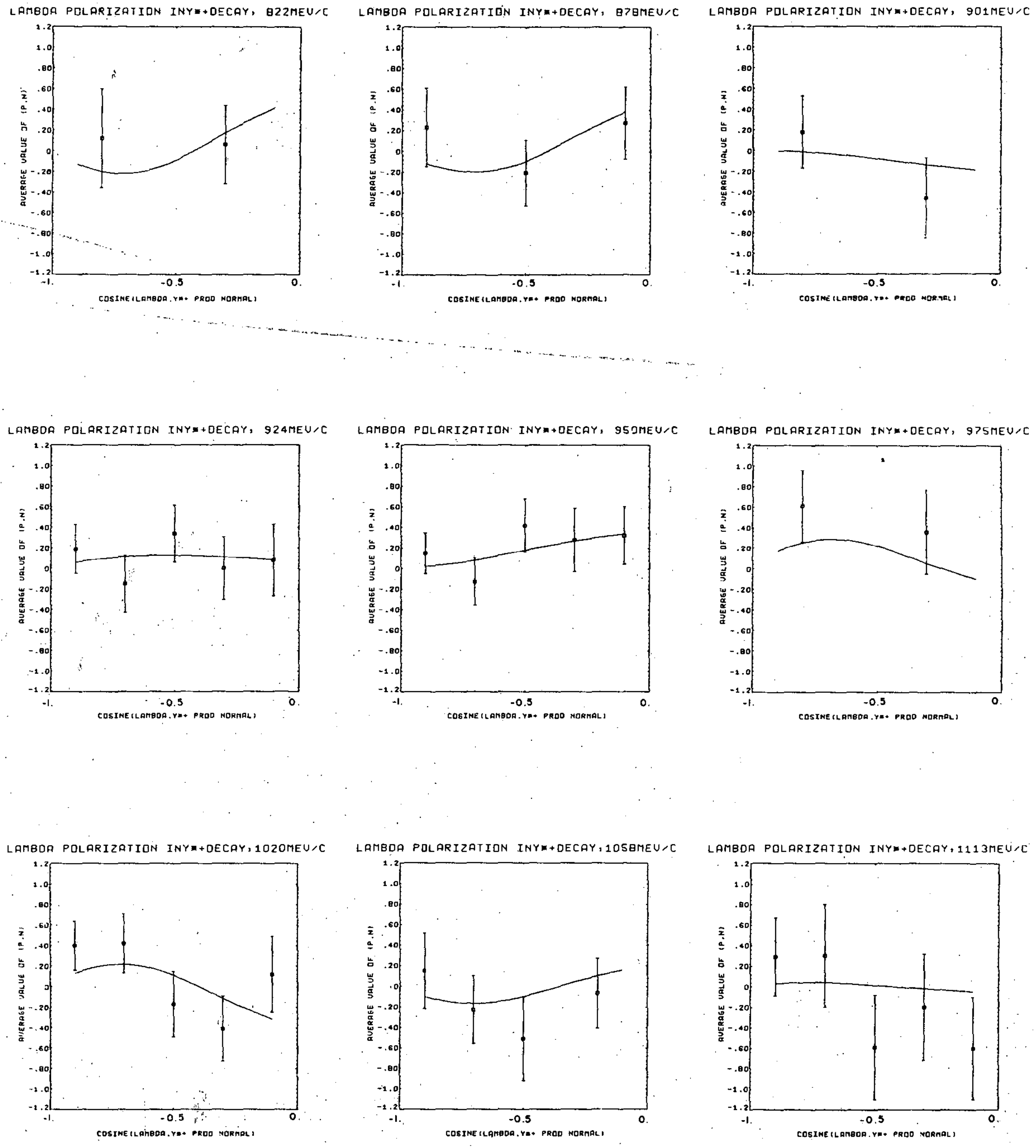

XBL 6811-6165

Fig. 12A

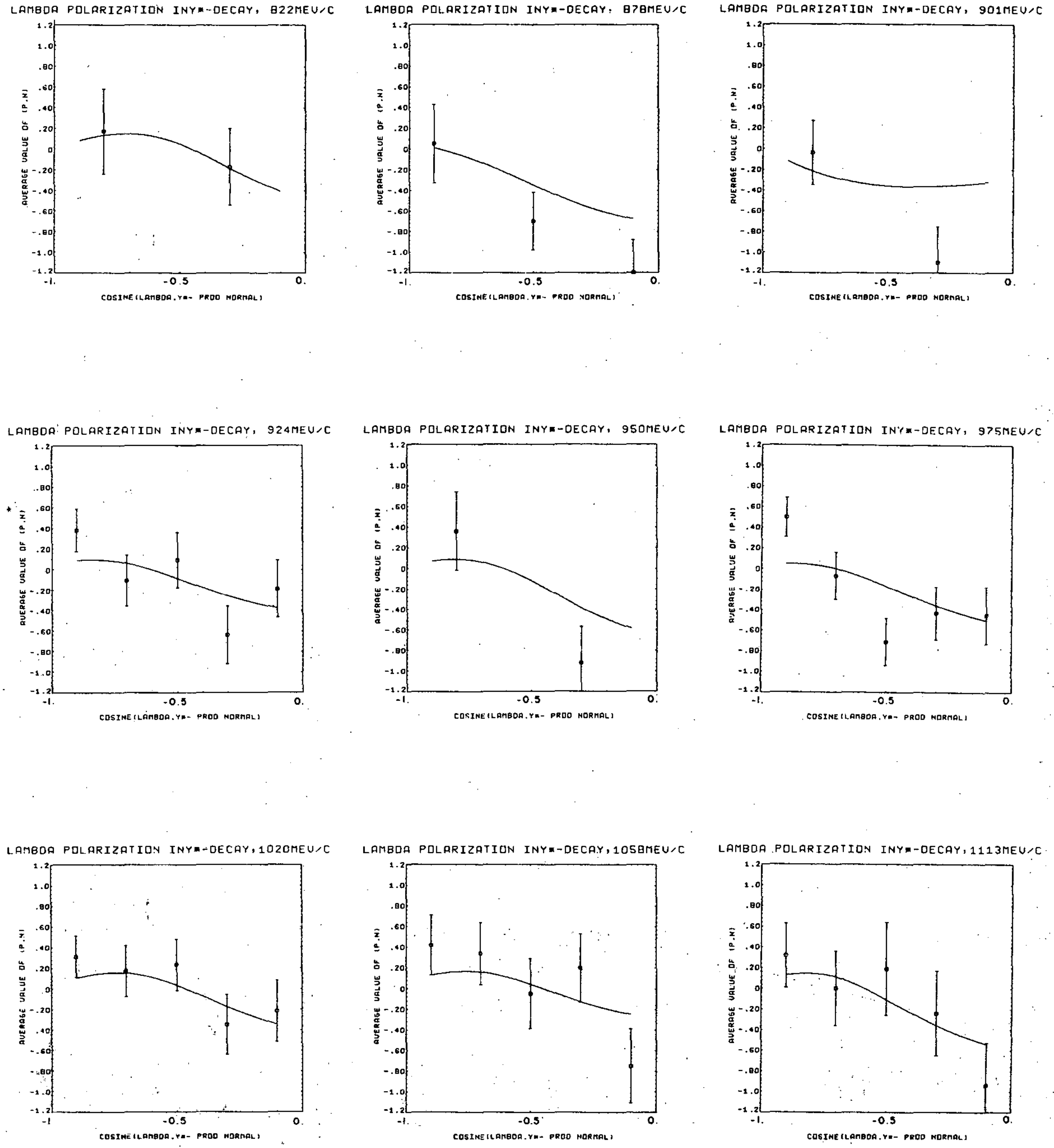

XBL 6811-6164

Fig. 12B

V. RESULTS FROM THE FITTED DATA

A. Mass of the $Y_1^*(1385)$

The best fit to the data was obtained when the masses of the $Y_1^{*\pm}(1385)$ were as shown in Table IV. The values of the masses were obtained by varying the positions of the Y_1^* bands with respect to the kinematic boundaries in the experimental Dalitz plot distributions (see Chapter IV, Section D). The errors quoted were obtained from the sensitivity of the chi-square of the fit to changes in the $Y_1^{*\pm}$ masses. The average values of the masses obtained were

$$Y_1^{*+}(1385) \quad : \quad (1384.2 \pm 1.4)\ \text{MeV}$$

and

$$Y_1^{*-}(1385) \quad : \quad (1387.8 \pm 1.2)\ \text{MeV}$$

and for the mass difference

$$(Y_1^{*-} - Y_1^{*+}) \quad : \quad (3.6 \pm 1.0)\ \text{MeV}$$

These values are in agreement with published results.[7] For the width used for the $Y_1^*(1385)$ see Appendix A.

B. Initial Fitting Results

As a first step fits were made with a small number of waves then progressively adding more and more waves. As described in Chapter IV, information from the Dalitz plot density, production angular distribution and lambda polarization were used simultaneously in the fitting. Using an initial guess for the values of the matrix elements $T_{0,1}$ for each wave included in the fit, the corresponding Dalitz plot density and Y^{*+}, Y^{*-} production and lambda polarization angular distributions were calculated from the model, and a chi-square was computed for the goodness of fit of the calculated distributions to the data. Then this chi-square was minimized by varying the $T_{0,1}$. This procedure was followed for every

Table IV. Measured mass of the $Y_1^*(1385)$.

Incoming Momentum GeV/c	Y_1^{*+} Mass MeV	Y_1^{*-} Mass MeV
822	1383.7 ± 2.0	1387.7 ± 2.0
878	1385.7 ± 2.0	1388.7 ± 2.0
901	1383.7 ± 2.0	1387.7 ± 2.0
924	1383.7 ± 1.5	1387.7 ± 1.0
950	1383.7 ± 2.0	1387.7 ± 1.5
975	1383.7 ± 1.5	1387.7 ± 1.0
1020	1384.7 ± 1.5	1387.7 ± 1.5
1058	1384.7 ± 1.5	1387.7 ± 1.5
1113	1384.7 ± 2.0	1387.7 ± 1.5

incoming momentum interval separately.

Three of the nine energy intervals in this experiment (corresponding to the K^- incoming momenta at 822, 901 and 950 MeV/c) contain very little data, see Chapter IV, Table III. For this reason these three energy intervals were treated in a manner slightly different from the rest (to be explained below).

In the initial attempts to fit the data with all partial waves up to FF5, poor convergence indicated a redundancy in the fitting expression. To reduce the number of parameters, waves having the same total angular momentum (J) and the same initial orbital state (L) but a different orbital angular momentum state (L′) between the produced Y_1^* and the spectator pion were constrained to have the same amplitude, but of course a different centrifugal barrier factor (see Chapter IV, Section C). The uniform background was fixed at ~20% (see Chapter IV, Section E).

Since only the relative phases between the different partial waves rather than their absolute phases are physically observable, the phase of one of the waves must be fixed.

The number of unknown parameters (N.P.) is equal to four times the number of waves minus one. The factor 4 signifies a complex unknown for each iso-spin state, and the subtraction of one comes from removing the absolute phase. The number of data points (N.D.P.) in the fitting procedure is the sum of the number of bins in the Dalitz plot distribution and the number of bins in Y^{*+} - and Y^{*-} - production angular distributions and the number of bins in the lambda polarization for Y^{*+} - and Y^{*-} - production, the number of bins in the Dalitz plot was such that no bin contains less than 15 events. The angular distributions are in 5, 10 or 20 equal intervals (in the cosine of the production angle for each Y^*) depending on the data available for each momentum, and the lambda polarization distributions were folded and grouped in five bins for each Y^* - production. The chi-square (χ^2) from a certain fit was used to calculate the confidence level (C.L.) for that fit by evaluating the following:

$$\text{C.L.} = \frac{1}{\sqrt{2\pi}} \int_y^\infty \exp\left(-\frac{x^2}{2}\right) dx$$

$$y = \sqrt{2\chi^2} - \sqrt{2(\text{ND})-1} \quad \text{for ND} \geq 30$$

where ND is the number of degrees of freedom which is equal to (N.D.P.-N.P.). Table V shows the confidence levels obtained from the initial fits. The main features in this table are that the lowest momentum interval can be fitted well with the waves PP1, DS3 and PP3; and when FP5 and DD5 are included they contribute little to the cross-section (see Table VI at 878 MeV/c). At the higher momenta, the waves FP5 and DD5 are important but not sufficient to fit the data. At the momenta 1020 and 1113 MeV/c the C.L. is not high enough to be significant for any of the trials in Table V, possibly because of a poor choice of bin sizes or the importance of high angular momentum waves which are not included in the fit.

Table VI contains the partial cross-sections for the partial waves included in trial number 8 in Table V. We note that at the K^--momentum 1058 MeV/c the waves PP1 and FP5 are the largest contributors to the cross-sections whereas at the K^- momentum 1113 MeV/c, PP1 (I=1) all but disappears and FP5 (I=0) is still the largest contributor to the cross-section. A statement similar to the above also holds for the wave PP3 (I=0) at the momentum 1020 MeV/c. These features will be discussed later on in this section.

One of the pitfalls encountered in using a minimization program of the sort utilized in this analysis is that the program may select the local minimum in the χ^2 surface which is closest to the starting values

Table V. Confidence levels for the initial fits. Background fixed at 20. per cent of the partial cross-section.

Trial Number											
	K^- momentum (MeV/c)					878	924	975	1020	1058	1113
	Bins in Dalitz Plot					24	36	43	36	36	26
	Bins in angular distribution					2(10)	2(10)	2(10)	2(10)	2(10)	2(10)
	Waves					Confidence Levels					
	PP1	DS3*	PP3	DD5	FP5**						
1				X	X	$(7.7)10^{-11}$	$(3.6)10^{-15}$	$(1.0)10^{-11}$	$(1.3)10^{-11}$	$(1.1)10^{-4}$	$(4.1)10^{-9}$
2		X		X	X	.092	$(5.2)10^{-5}$	$(5.5)10^{-4}$	$(9.5)10^{-4}$	0.021	$(4.2)10^{-5}$
3			X	X	X	.036	$(7.6)10^{-4}$	$(6.1)10^{-3}$	$(5.2)10^{-4}$	$(4.9)10^{-3}$	$(1.2)10^{-5}$
4	X		X	X	X	0.036	$(3.2)10^{-3}$	0.053	$(7.0)10^{-3}$	0.22	$(4.7)10^{-6}$
5		X	X	X	X	0.081	$(3.2)10^{-4}$	0.011	$(3.7)10^{-3}$	0.026	$(1.2)10^{-5}$
6	X	X	X	X		0.23	$(1.7)10^{-3}$	0.062	$(1.7)10^{-3}$	0.014	$(1.4)10^{-6}$
7	X	X	X			0.38	$(5.6)10^{-5}$	$(1.7)10^{-3}$	$(1.8)10^{-8}$	$(1.1)10^{-3}$	$(8.9)10^{-11}$
8	X	X	X	X	X	0.15	$(1.2)10^{-3}$	0.14	$(2.7)10^{-3}$	0.41	$(3.9)10^{-6}$

* Indicates that DD3 with the same amplitude is included without increasing the number of parameters.

** Indicates FF5 is included without increasing the number of parameters.

Table VI. Partial cross-sections in millibarn $\sigma(K^-p \rightarrow \Lambda\, \pi^-\pi^+)$ for the waves used in Table V trial number 8. The symbols I_0, I_1, indicate the iso-spin.

K^- Momentum MeV/c		878	924	975	1020	1058	1113
Confidence Level		0.15	$(1.2)10^{-3}$	0.14	$(2.7)10^{-3}$	0.41	$(3.9)10^{-6}$
PP1	I_1	0.36±.12	0.18±.08	0.22±.09	0.22±.07	1.03±.16	0.05±.04
	I_0	0.26±.09	0.40±.09	0.53±.10	0.30±.10	0.40±.13	0.42±.20
DS3	I_1	0.67±.16	0.05±.05	0.27±.10	0.12±.07	0.03±.05	0.10±.04
	I_0	0.11±.09	0.17±.08	0.24±.11	0.09±.06	0.14±.08	0.38±.20
PP3	I_1	0.12±.07	0.003±.01	0.004±.02	0.28±.08	0.32±.17	0.07±.07
	I_0	0.62±.13	0.42±.09	0.09±.07	0.95±.16	0.11±.1	0.05±.05
DD3*	I_1	0.09	0.008	0.005	0.02	0.006	0.02
	I_0	0.02	0.02	0.004	0.02	0.03	0.09
DD5	I_1	0.02±.03	0.40±.13	0.72±.12	0.09±.05	0.31±.17	0.24±.08
	I_0	0.01±.02	0.10±.06	0.008±.02	0.42±.10	0.15±.08	0.14±.09
FP5*	I_1	0.06±.04	0.39±.12	0.34±.09	0.18±.08	0.04±.07	0.02±.03
	I_0	0.04±.05	0.26±.07	0.15±.08	0.14±.06	0.61±.17	1.11±.28
FF5	I_1	.002	0.01	0.02	.001	0.002	0.001
	I_0	.0007	0.006	.005	.0005	0.03	0.06
Background		0.68	0.57	0.70	0.86	0.86	0.67

* see Table V.

"initial guess" of the parameters. Precautions were taken to escape this; first by repeating the fitting procedure with different starting values; and second by allowing the program, after finding a minimum, to move randomly to another point on the chi-square surface and repeat the minimization. In every case we arrived at a solution giving values of the parameters which were consistent with the other trials.

Attempting to improve the confidence levels, we tried different bin sizes in the angular distributions and Dalitz plots. In some cases the solutions gave a better confidence level than in Table V. In Table VII we give the values of the confidence levels obtained in one of the trials of this procedure. The contributions to the partial cross-section from each of the partial waves used are listed in Table VIII. Comparing the solutions in Table VIII with those in Table VI, one sees that even though the corresponding confidence levels for some of the momentum intervals have decreased slightly the solutions from these two tables are consistent within errors. We also notice upon comparison of the two above solutions at the momentum interval 1058 MeV/c that the cross-section for the wave PP1 (I=1) has changed by 0.33 m.b. (this will be discussed below). The values listed in Table VIII also show that some of the waves contribute large amounts to the partial cross-section but with large errors; for example PP1 and PP3 at 1058 MeV/c, and DS3 and FP5 at 1113 MeV/c. This implies that the chi-square surface has a shallow minimum with respect to these parameters. Thus to determine whether such large values of these waves are needed or not, we go back for a second look at the initial fit shown in Table V. For example, comparing trials 5 and 6 at 1058 MeV/c in Table V we see that trial 5 (DS3, PP3, DD5, FP5) is a better fit than trial 6 (PP1, DS3, PP3, DD5) by almost a factor of two in the confidence level. By arguments similar to the above and by invoking continuity between adjacent momentum intervals

Table VII. Confidence levels obtained by optimizing bin sizes in the data. Waves included in the fit are PP1, DS3, PP3, DD5, FP5, DD3 and FF5. Background fixed around 20%.

K^- Momentum in MeV/c	Bins in Dalitz Plot	Bins in Angular Distribution	Confidence Level
878	15	2(10)	0.068
924	27	2(20)	0.17
975	32	2(20)	0.16
1020	28	2(20)	0.065
1058	23	2(10)	0.12
1113	17	2(5)	0.008

Table VIII. The partial cross-section $\sigma(K^- p \to \Lambda \pi^+ \pi^-)$ in millibarn for the waves used in the fit of Table VII. The symbols I_1 and I_0 indicate the iso-spin state.

K^- Momentum MeV/c		878	924	975	1020	1058	1113
Confidence Level		0.068	0.17	0.16	0.065	0.12	0.008
PP1	I_1	0.47±.18	0.11±.07	0.39±.12	0.15±.10	0.70±.51	0.14±.11
	I_0	0.37±.16	0.46±.08	0.56±.12	0.57±.18	0.64±.41	0.11±.11
DS3	I_1	0.48±.15	0.11±.05	0.19±.14	0.27±.17	0.008±.04	0.10±.10
	I_0	0.10±.09	0.02±.03	0.22±.12	0.09±.10	0.20±0.20	0.44±.19
PP3	I_1	0.11±.10	0.01±.02	0.03±.04	0.34±.26	0.26±.24	0.14±.16
	I_0	0.65±.27	0.54±.13	0.10±.09	0.43±.26	0.40±.30	0.10±.12
DD3*	I_1	0.07	0.02	0.04	0.05	0.002	0.02
	I_0	0.01	0.004	0.04	0.02	0.04	0.10
DD5	I_1	0.02±.04	0.50±.10	0.69±.24	0.21±.15	0.31±.24	0.34±.30
	I_0	0.01±.02	0.12±.07	0.05±.09	0.41±.14	0.16±.19	0.13±.12
FP5	I_1	0.07±.09	0.25±.10	0.32±.12	0.12±.08	0.05±.09	0.007±.03
	I_0	0.02±.04	0.23±.06	0.08±.06	0.17±.09	0.44±.25	0.99±.68
FF5*	I_1	0.002	0.009	0.01	0.006	0.003	0.005
	I_0	0.0004	0.006	0.003	0.006	0.02	0.05
Background		0.69	0.57	0.70	0.85	0.86	0.73

* The amplitudes for DD3 and FF5 are constrained to be the same as the amplitudes for DS3 and FP5 respectively, with the appropriate centrifugal barrier.

we tried to improve the fits at the momenta 1020, 1058 and 1113 MeV/c by fixing the values of some of the parameters. The values of the fixed parameters are not arbitrary, but consistent with previous solutions (Table VI) and with adjacent momentum intervals. Table IX shows the improved solutions obtained by fixing some of the parameters and the values at which they were fixed.

In summary, our procedure for finding the best solution consists of the following steps; first we fit each energy interval using different partial waves to find what waves are needed, second we try to improve these fits by binning the data in different ways, and third by comparing adjacent energy intervals we improve these fits further by fixing the values of some of the parameters; thus having essentially a feedback procedure which is repeated until a satisfactory fit is obtained.

Three of the momentum intervals in this experiment (822, 901, 950 MeV/c) contain very little data (approximately 250 events each, see Table I, Chapter II). These data may be sufficient to do certain types of analyses, but for the analysis used here such a small amount of data leads to inconclusive results. However by using the solutions we obtained for the momenta (878, 924 and 975 MeV/c) which are adjacent to poorly populated intervals we got plausible solutions for the latter.

C. Properties of the Best Fit

The set of best fits chosen consists of the fit from Table VI for the momentum interval 878 MeV/c, the fits from Table VIII for the momenta 924 and 975 MeV/c and the fits from Table IX for the momenta 1058 and 1113 MeV/c. At 1020 MeV/c, of the two solutions included in Table IX we chose the solution with the higher confidence level. At the momentum 1058 MeV/c, the fit chosen is preferred over others, which may have a higher confidence level, on the basis of continuity arguments between

Table IX. Improved solutions obtained by fixing some of the parameters as described in the text. The partial cross-sections in m.b. are given for each partial wave for the reaction ($K^-p \rightarrow \Lambda\pi^+\pi^-$). The values in square brackets are fixed. The background is fixed at ~20%.

K^- Momentum MeV/c		1020	1058	1113	1020
Bins in Dalitz Plot		21	28	17	30
Bins in Angular Distribution		2(10)	2(10)	2(5)	2(20)
Confidence Level		0.08	0.11	0.01	0.19
Waves		Cross-sections in Millibarn			
PP1	I_1	0.19±.14	[0.14]	0.17±.16	[0.15]
	I_0	0.16±.10	[0.31]	0.12±.11	[0.31]
DS3	I_1	0.16±.06	0.19±.11	0.08±.08	0.38±.09
	I_0	0.19±.08	0.09±.06	[0.20]	0.39±.14
PP3	I_1	0.03±.05	[0.28]	0.22±.20	0.27±.09
	I_0	0.50±.20	[0.11]	0.13±.12	[0.11]
DD3*	I_1	0.03	0.04	0.02	0.07
	I_0	0.04	0.02	0.05	0.08
DD5	I_1	0.12±.06	0.19±.11	0.44±.15	0.59±.13
	I_0	0.10±.06	0.04±.05	0.13±.13	0.005±.01
FP5	I_1	0.48±.14	0.54±.18	0.002±.02	0.27±.08
	I_0	[0.87]	1.20±.17	1.11±.28	0.24±.10
FF5*	I_1	0.03	0.03	0.0001	0.01
	I_0	0.03	0.05	.06	0.009
Background		0.75	0.86	0.70	0.75

* See Table VIII.

adjacent momentum intervals. The same arguments of continuity apply to the choice of a fit at the momentum interval 1020 MeV/c.

It is observed that the values at which the background is fixed do not decrease with increasing momentum as they might if the background is S-wave phase space. However the background is used here to account also for processes, other than S-wave phase space,[22] which were not considered in the model described in Chapter III.

If the background is allowed to vary in the fitting procedure it remains at approximately 20% for the momenta 924, 975, 1020 and 1058 MeV/c but increases to between 30 and 40 percent at 878 and 1113 MeV/c. This increase could be explained by the small amount of data available at the two latter momenta. See Table III, Chapter IV.

Table X contains the confidence levels and the partial cross-sections for the waves used in the best solution and Table X-A gives the corresponding chi-squares. Table X-B gives the phases of the partial waves in the momentum intervals which contain a large amount of data. One of the phases in each momentum interval is fixed in order to remove the ambiguity of an absolute phase, while all other phases, including those belonging to waves in square brackets in Table X were allowed to vary. Thus there is a slight difference between Tables XI and X-B. In Table XI some phase differences from the best solution are listed, see Section D below.

Figure 13 is a plot of the partial cross-section for each of the partial waves as a function of beam momentum; the values of the parameters which were fixed are plotted without error bars. The values of the parameters from the best solution were used to calculate the projections of the Dalitz plot density upon the $(\Lambda\pi^+)$ and $(\Lambda\pi^-)$ mass squared axes. These are shown in Fig. 14a,b superposed over the corresponding experimental histograms. Even though these histograms were not used explicity in the

Table X. Cross-sections and confidence levels for the best solutions. Quantities in square brackets are fixed and I_1, I_0 indicate iso-spin state.

K^- Momentum MeV/c		822	878	901	924	950	975	1020	1058	1113
Bins (Dalitz Plot)		11	24	12	27	13	32	30	28	17
Bins (Angular Distribution)		2(10)	2(10)	2(10)	2(20)	2(5)	2(20)	2(20)	2(10)	2(5)
Confidence Level		0.02	0.15	0.04	0.17	0.004	0.16	0.19	0.11	0.01
Waves		Partial Cross-Section Millibarn								
PP1	I_1	0.03±.10	0.36±.12	0.05±.06	0.11±.07	0.49±0.48	0.39±.12	[0.15]	[0.14]	0.17±.16
	I_0	0.05±.09	0.26±.09	0.49±.36	0.46±.08	0.16±.20	0.56±.12	[0.31]	[0.31]	0.12±.11
DS3	I_1	0.47±.23	0.67±.16	0.02±.05	0.11±.05	0.39±.24	0.19±.14	0.38±.09	0.19±.11	0.08±0.08
	I_0	0.006±.03	0.11±.09	0.79±.40	0.02±.03	0.21±.31	0.22±.12	0.39±.14	0.09±.06	[0.20]
PP3	I_1	0.77±.34	0.12±.07	0.50±.39	0.01±.02	0.45±.21	0.03±.04	0.27±.09	[0.28]	0.22±.20
	I_0	0.80±.30	0.62±.13	0.44±.18	0.54±.13	0.06±.11	0.10±.09	[0.11]	[0.11]	0.13±.12
DD3*	I_1	0.05	0.09	0.004	0.02	0.07	0.04	0.07	0.04	0.02
	I_0	0.0007	0.02	0.01	0.004	0.04	0.04	0.08	0.02	0.05
DD5	I_1	[0.01]	0.02±.03	0.008±.02	0.50±.10	[0.80]	0.69±.24	0.59±.13	0.19±.11	0.44±.15
	I_0	[0.006]	0.01±.02	0.04±.05	0.12±.07	0.00±.01	0.05±.09	0.005±.01	0.04±.05	0.13±.13
FP5	I_1	[0.06]	0.06±.04	[0.06]	0.25±.10	0.01±0.04	0.32±.12	0.27±.08	0.54±.18	0.002±.02
	I_0	[0.02]	0.04±.05	[0.02]	0.23±.06	0.08±.10	0.08±.06	0.24±.10	1.20±.17	1.11±.28
FF5*	I_1	0.001	0.002	0.002	0.009	0.0006	0.01	0.01	0.03	0.001
	I_0	0.0002	0.0007	0.0004	0.006	0.002	0.003	0.009	0.05	0.06
Background		0.54	0.68	0.71	0.57	0.47	0.70	0.75	0.86	0.70

* Implies constraining the amplitudes such that (DD3=DS3) and (FF5=FP5) with the proper centrifugal barrier.

Table X-A. Chi-squares for the best solution.

K^- Momentum MeV/c	Number of Parameters	Number of Bins	Number of Degrees of Freedom	Chi-square	Confidence Level
822	11	41	30	47.5	0.02
878	19	54	35	43.5	0.15
901	15	42	27	40.6	0.04
924	19	77	58	68.0	0.17
950	18	33	15	31.6	0.004
975	19	82	63	74.0	0.16
1020	14	80	66	76.0	0.19
1058	12	58	46	58.0	0.11
1113	17	37	20	36.1	0.01

Table X-B. Phase angles in degrees. The fixed phase at each energy is in brackets.

Momentum MeV/c		878	924	975	1020	1058	1113
Wave	Iso-spin						
PP1	1	(90)	181±21	8±20	47±37	248±35	39±32
	0	207±11	297±14	123±21	288±37	337±35	56±48
DS3	1	171±9	270±13	53±25	218±35	93±28	99±35
	0	304±20	149±31	337±24	351±56	215±24	300±20
PP3	1	96±21	196±23	300±40	276±38	121±16	165±13
	0	85±8	(180)	(0)	(0)	(0)	(0)
DD5	1	178±49	269±4	67±18	319±37	355±21	79±15
	0	51±63	15±7	8±34	330±84	284±28	324±17
FP5	1	358±23	194±8	36±19	228±51	38±22	73±360
	0	276±30	334±10	179±28	159±49	159±21	242±19

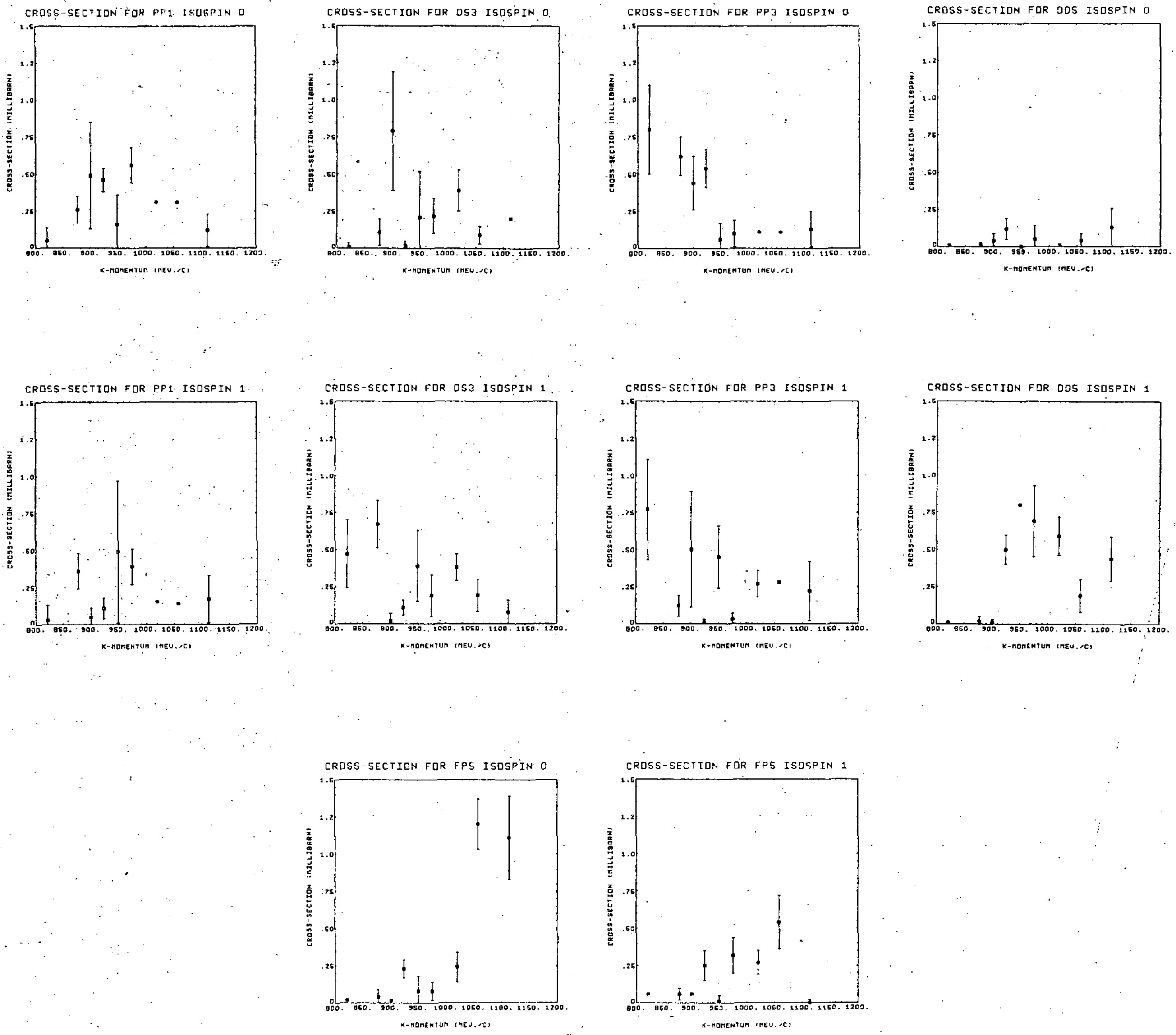

Fig. 13

XBL 6811-6166

fitting procedure, the calculated curves fit them fairly well. The reason that the calculated curves in Fig. 14a, b are not shown for parts of the allowed mass-range, was that the corresponding regions of the Dalitz plot were poorly populated and were not used in the fitting procedure. Chi-squares for the goodness of fit of these curves to the histograms are shown in Table XII.

The experimental angular distributions are shown in Fig. 15a,b the smooth curves are from the best solutions. The decay angular distributions of the $Y_1^{*\pm}(1385)$ were calculated using the values of the best solution, and were plotted as the smooth curves superposed over the experimental histograms in Fig. 9a,b. The results of the fit for the lambda polarization at the different momentum intervals are shown as the smooth curves in Fig. 12a,b.

D. Structure in the Partial Wave Amplitudes

The cross-section for the wave DD5 (I=1) shows the resonant structure corresponding to the $(5/2^-)$ $Y_1^*(1770)$ and the cross-section for the wave FP5 (I=0) shows the structure corresponding to the $(5/2^+)$ $Y_0^*(1820)$. The cross-section for the wave PP3 (I=0) has a shape that resembles the high mass part of a resonance shape. If this wave is resonating,[33] it will correspond to a state of mass near or below the lower end of the energy range in this experiment (1700 MeV) and iso-spin, spin and parity of $0(3/2^+)$.

The relative phases of these waves are meaningful, in the fitting procedure of this experiment, when they contribute a statistically meaningful amount to the cross-section. From Fig. 13 we note that the waves PP3 (I=0) and DD5 (I=1) are both large at the momentum interval 975 MeV/c; and the waves DD5 (I=1) and FP5 (I=0) are both large at the momentum intervals 1020, 1058 and 1113 MeV/c. The phase angle DD5 (I=1)

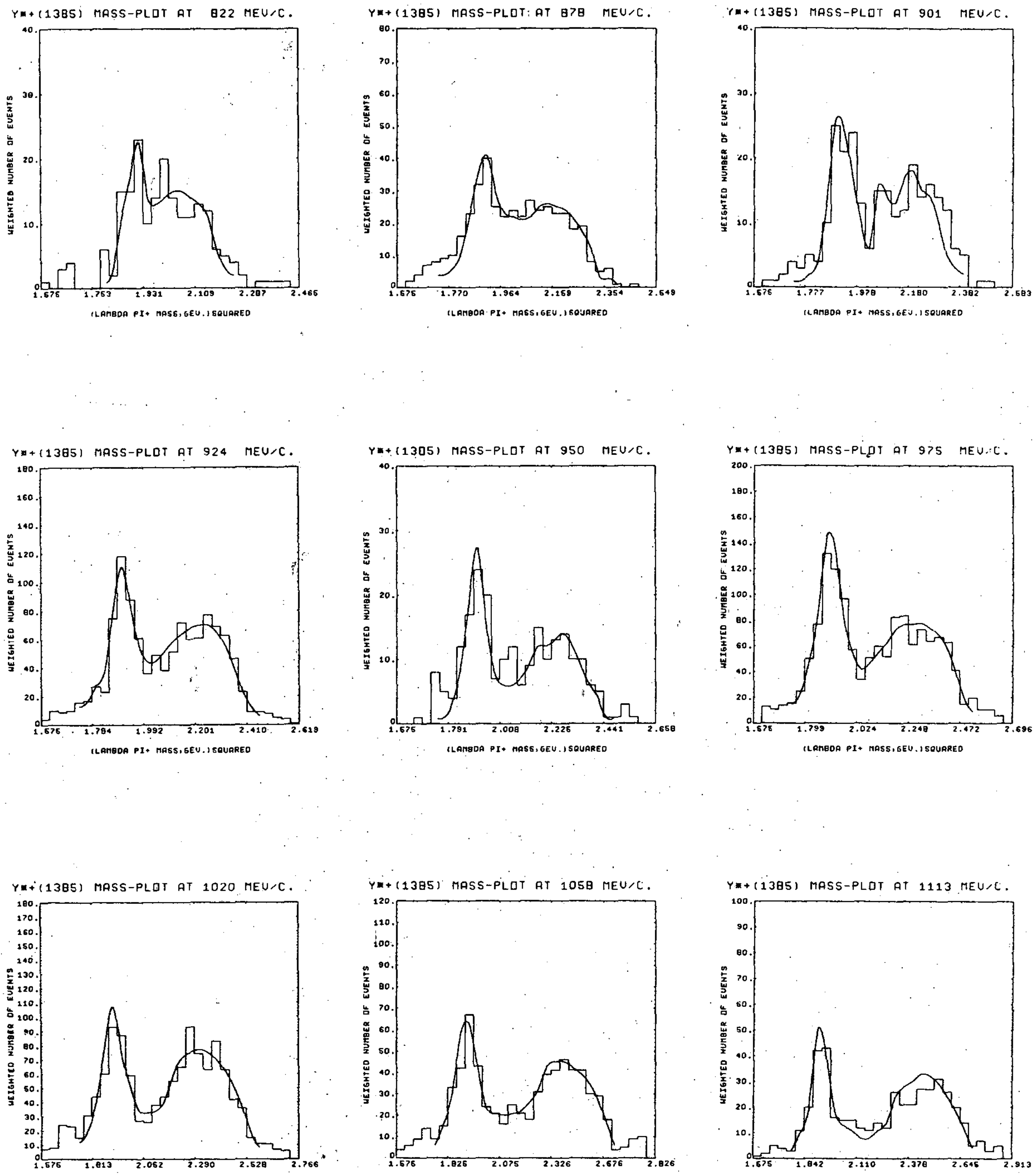

XBL 6811-6155

Fig. 14A

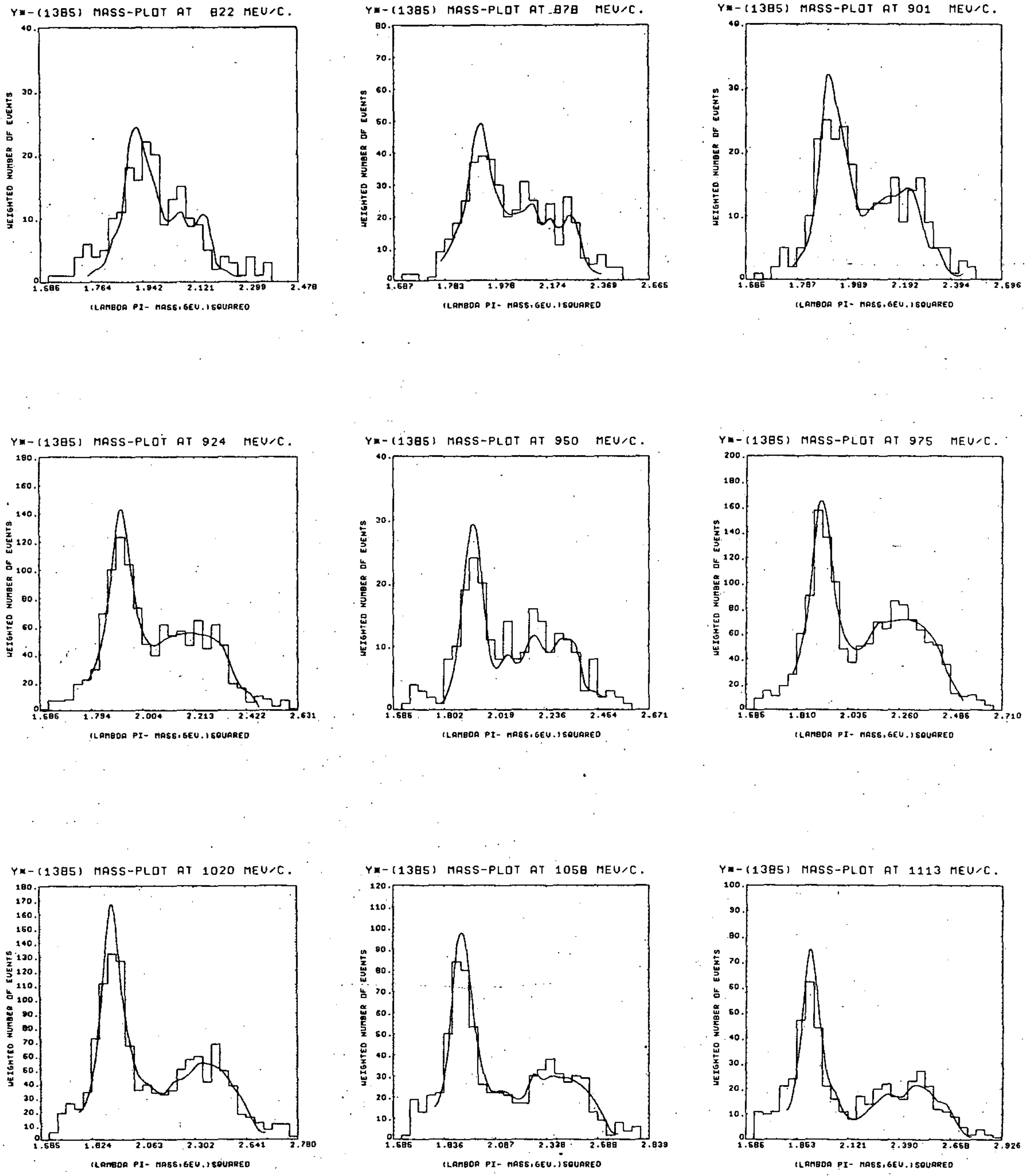

XBL 6811-6158

Fig. 14B

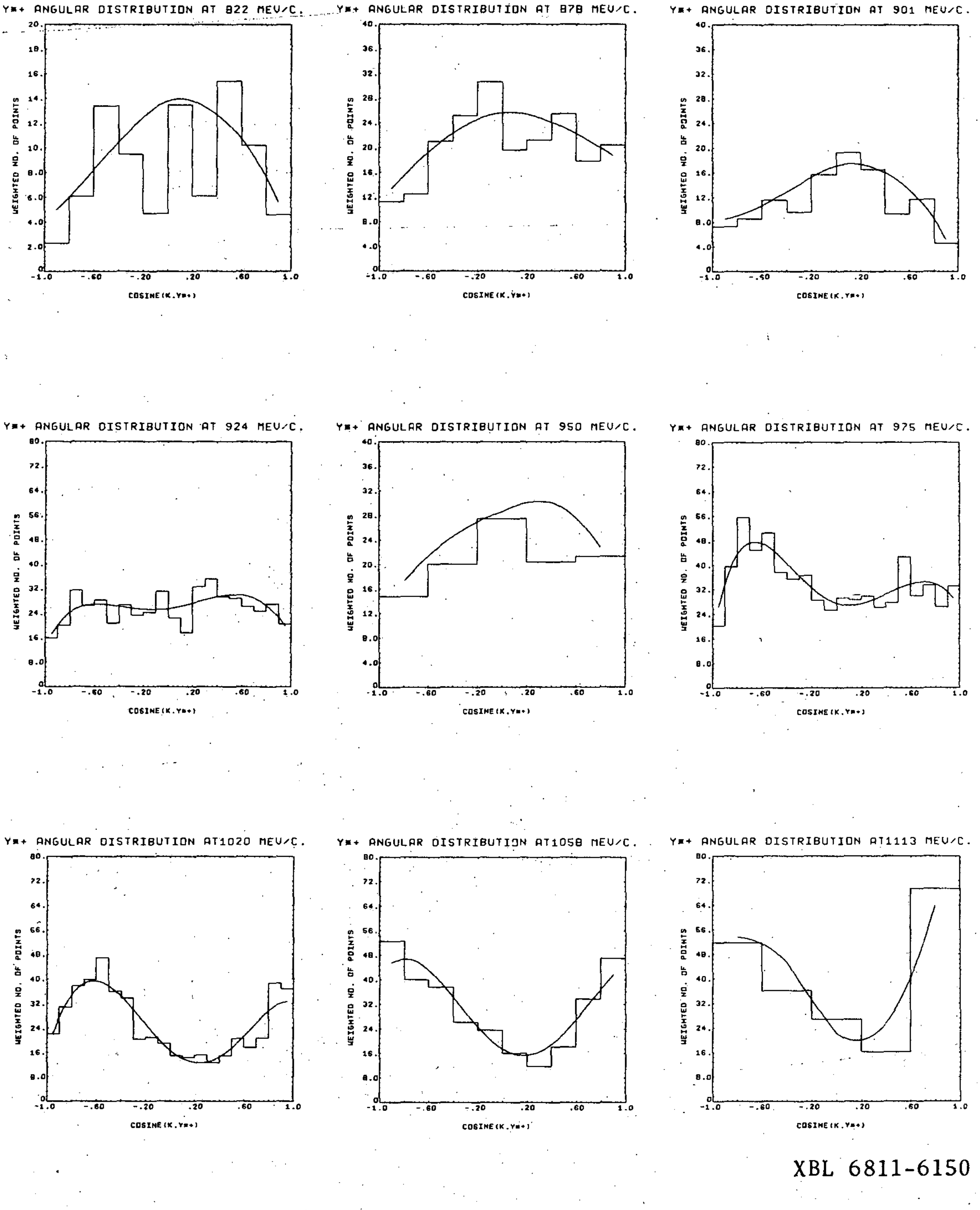

XBL 6811-6150

Fig. 15A

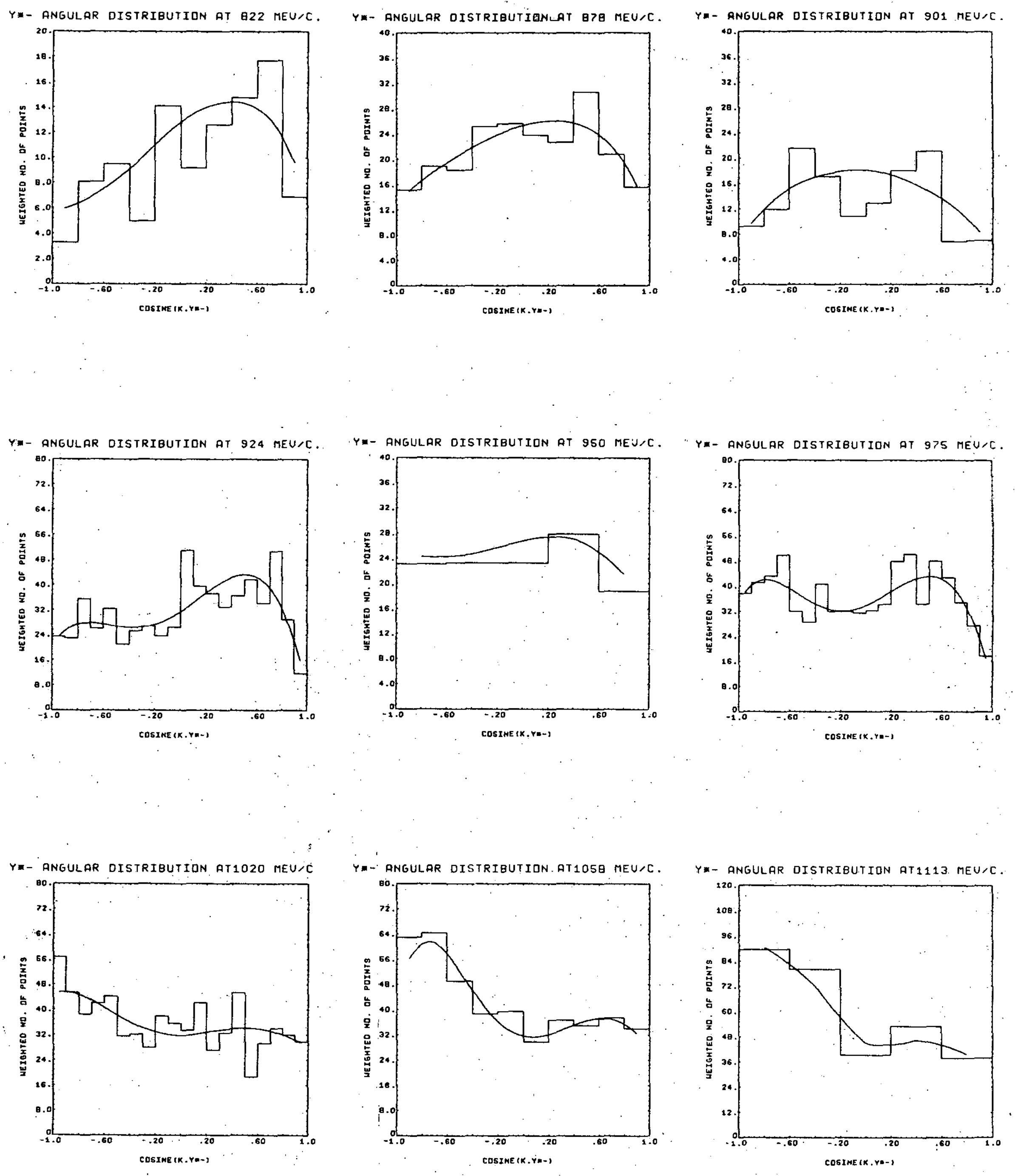

XBL 6811-6151

Fig. 15B

Table XI. Relative phases in degrees.

K^- Momentum MeV/c	878	925	975	1025	1058	1113
DD5(I=1)-PP3(I=0)	93±50	90±14	67±30	--	--	--
FP5(I=0)-DD5(I=1)	--	--	112±19	201±14	136±19	167±25

Table XII. Chi-square values for the fit of the mass-projection on the Y_1^{*+}, Y_1^{*-}(1385) axes compared to the experimental histogram.

K^- Momentum MeV/c	Y^{*+} Number of Points	Y^{*+} χ^2	Y^{*-} Number of Points	Y^{*-} χ^2
822	16	11	19	23
878	22	20	21	18
900	21	14	20	17
925	22	21	21	26
950	22	30	20	28
975	22	19	21	21
1025	22	37	21	35
1058	22	14	21	16
1113	22	16	21	22

PP3 (I=0) at 975 MeV/c is (90 ± 14) degrees, and at the momenta 1020, 1058 and 1113 MeV/c the phases FP5 (I=0)-DD5 (I=1) are (201 ± 14), (136 ± 19) and (167 ± 25) degrees respectively, see Table XI. These phases show that the resonant states $Y_1^*(1770)$ and the $Y_0^*(1820)$ have the opposite sign imaginary parts at resonance.

The phase between PP3 (I=0) and DD5 (I=1) also suggests that the PP3 (I=0) wave might be resonating; for if we remember the Wigner condition (that the phase of a resonating amplitude increases counter-clockwise on a complex plane) then far below the mass of the $Y_1^*(1770)$, the amplitude for the DD5 (I=1) wave will be mainly real; thus a phase of (90 ± 14) degrees between this wave and the PP3 (I=0) wave makes the latter mainly imaginary. Therefore we conclude from the best solution that the wave PP3 (I=0) has a large and mainly imaginary amplitude in the reaction $K^-p \rightarrow Y_1^*(1385) + \pi \rightarrow \Lambda\, \pi^+\pi^-$ at the center of mass energy of ~1700 MeV.

If the contribution to the total cross-section of the resonances $Y_0^*(1820)$ and $Y_1^*(1770)$ in the K^-p interaction were known, then with the information we have from this experiment the branching fraction of these two states into the channel $Y_1^{*\pm}\pi^{\mp}$ could be calculated. Cool et al.[8] measured the total cross-sections in the reactions K^-p and K^-d in the energy region where the above resonances appear, and by comparison of these two cross-sections, they found the energy dependence of the total cross-section in the iso-spin states 0 and 1 separately. Using their results we estimate that the $Y_1^*(1770)$ contributes (20.0 ± 3.0) m.b. to the iso-spin 1 cross-section and the $Y_0^*(1820)$ contributes (30.0 ± 3.0) m.b. to the iso-spin 0 cross-section at the respective central mass-values of these resonant states.[35] Using these values in conjunction with the results of this experiment for the waves DD5 (I=1) and FP5 (I=0) we calculate the branching ratios as: (K^-p is a mixture of I=0 and I=1 states)

$$\frac{K^-p \rightarrow Y_1^*(1770) \rightarrow Y_1^{*\pm}(1385) + \pi^{\mp}}{K^-p \rightarrow Y_1^*(1770) \rightarrow \text{all}} = (8.0 \pm 3.3)\%$$

$$\frac{K^-p \rightarrow Y_0^*(1820) \rightarrow Y_1^{*\pm}(1385) + \pi^{\mp}}{K^-p \rightarrow Y_0^*(1820) \rightarrow \text{all}} = (8.0 \pm 1.4)\%$$

These values are in agreement with References 37.

The variation as a function of energy of the cross-section for the wave DD5 (Fig. 13) was fit to a Breit-Wigner shape curve. (See Appendix C). The mass and width of the $Y_1^*(1770)$ from this fit are (1775 ± 5) MeV and (55 - 5 + 15) MeV. This is a crude fit because there are only a few data points with large errors. In Reference 34, the values of the mass and width by Armenteros et al. are 1766 ± 4 and 114 ± 8 MeV and those by Smart are 1775 ± 7 and 146 ± 9 MeV. The mass values are in agreement with ours, but not the widths. However values for the width published previous to Reference 34 are in agreement with ours (see Reference 7).

The $Y_0^*(1820)$ appears near the upper end of the energy region in this experiment, therefore data are needed at higher energies before one can fit the $Y_0^*(1820)$ resonance shape to a Breit-Wigner curve.

E. Discussion

Armenteros et al.[34,36] analyzed the reaction $K^-p \rightarrow K^-p$, $K^-p \rightarrow \bar{K}^0n$ and $K^-p \rightarrow \Sigma\pi$ in the mass region 1.6 to 1.9 GeV. They carried out a partial wave analysis and found that, in order to fit the data, they needed resonant states in the S_{01}, D_{03}, D_{13}, D_{05} and F_{07} together with the previously mentioned $Y_0^*(1820)$ and $Y_1^*(1765)$. In some of their fits (Ref. 37) they also used fixed values of the masses, widths and elasticities of the states $5/2^+$ $Y_1^*(1910)$, $7/2^+$ $Y_1^*(2040)$ and $7/2^-$ $Y_0^*(2100)$. The masses of the S_{01}, D_{03}, D_{13}, D_{05} and F_{07} states were given as 1163 ± 3, 1696 ±3, 1668 ± 3, 1807 ± 10 and 1864 ± 2 MeV respectively. The elasticities were 0.14 ± .04, 0.18 ± .03, 0.09 ± .02, 0.09 ± .01 and 0.12 ± .02 respectively. The $\Sigma\pi$ branching fractions were 0.45 ± .25, 0.60 ± .12, 0.49 ± .11 and 0.25 respectively for the first four states above.

In a counter experiment by Bugg et al.[38], the total cross-section for K^-p and K^-d were measured for the laboratory momentum region 0.6 to 2.65 GeV/c. Unfolding the Fermi motion in the deuteron they separated the iso-spin states 0 and 1. They were able to fit their cross-sections using resonant states of constant widths and a momentum dependent background. Beside the established states some of these resonant states seem to correspond to those found by Armenteros et al. above, namely: I=1 state of mass 1665 ± 5 MeV and I=0 states of masses 1695 ± 4 MeV and 1870 ± 5 MeV. The fit to the data of Bugg et al. is not unique and some of their assumptions are 'simplistic', to use their own term.

The small elasticities and the large $\Sigma\pi$ branching fractions for the states S_{01}, D_{03}, D_{13} and D_{05} (in the convention of this paper $SD1_0$, $DS3_0$, $DS3_1$ and $DD5_0$)lead to the conclusion that the contributions of these states to the reaction $K^-p \rightarrow Y_1^*(1385) + \pi$ are small, in fact they are of the order of magnitude of the errors on the cross-sections in Table X. Thus if these resonant states exist, the fact that they are not detected in this experiment is not surprising. The state F_{07} beside having a small elasticity (0.12 ± .02) has a resonant mass above the energy region in this experiment, and its decay to $Y_1^*(1385) + \pi$ must be through F- or H- wave. Thus more data at higher energies are needed to detect this state in this channel.

APPENDICES

A. Experimental Chi-Square Distributions

Chi-square distributions for kinematically fitted events in bubble chamber experiments are known to be wider than the theoretical distributions by a factor α^2 that ranges between 1.6-2.0, and have a tail which is ~10% higher.[11,12] This effect is generally due to under-estimated errors in reconstruction programs. Before associating a probability level with the experimental value of chi-square we must take into account this stretching factor α^2. Reference 12 had analyzed the same type of event in the propane bubble chamber and used the same constraining programs as in this experiment, and found a stretching factor 2.4 for four degrees of freedom fit. The stretching factor does not seem to depend on the number of constraints (degrees of freedom).[11]

We give the following summary of our study of the experimental chi-square distribution:

1. For one-constraint fit at the vee decay vertex constrained to Λ, 8.5% of the events lie beyond the theoretical 2.5% level.

2. For three-constraint fit at the vee vertex constrained to a Λ pointing to the interaction origin, 11.4% of the events lie beyond the theoretical 5% level.

3. For seven-constraint fit for two prong and a vee constrained to $(K^- p \rightarrow \Lambda \pi^- \pi^+)$ 31% and 22% of the events lie beyond the theoretical 5% and 2% levels respectively.

B. Summary of Theoretical Details

Following Deler and Valladas[16] we will briefly discuss the procedure with which we arrive at the form of the amplitude given in Chapter III-B. The reader may refer to the above authors for a more complete description.

Restricting ourselves to the production of only one intermediate subsystem, one iso-spin state and one combination of spin-projections $M_i M_f^*$, and using the definition of symbols as in Chapter III-B, we write the amplitude: (T, transition matrix)

$$< \pi_1(\pi_2\Lambda)|T|\ KP >_{M_i M_f^*} = < q_1 q_1^* M_f^* \ |T|\ \bar{q}_i M_i >$$

$$= \sum_{JLL'} < q_1 q_1^* M_f^* |JM,L'j > T_{j\ell}^{JLL'}(W,w_1) < JM,LS|\bar{q}_i M_i >$$

since $T_{j\ell}^{JLL'}$ connects the two states $|JM,L'j>$ and $|JM,LS>$, where S is the spin of the initial nucleon.

Introducting helicity states, we have

$$|\bar{q}_i M_i> = \sum_{\lambda_i} |JM\lambda_i > < JM\lambda_i|\bar{q}_i M_i >$$

$$|JM,L'j> = \sum_{\lambda} |JMj\lambda > < JMj\lambda\ |JM,L'j >$$

since eigenstates of helicity form a basis.[23]

The conection between helicity states and spin total-angular momentum eigenstates is by the following (or similar forms) in the center of mass system of two particles:

$$< JM,LS|JM\lambda_1\lambda_2 > = (-1)^{2S+J-L+\lambda}\ C_{\lambda\,-\lambda\,0}^{SJL}\ \ C_{\lambda_1\ -\lambda_2\,\lambda}^{S_1 S_2 S}$$

$\lambda = \lambda_1 - \lambda_2$; S_1, S_2 are spins of particles one and two. The C's are Clebsh-Gordan coefficients:

$$C_{m_1 m_2 M}^{j_1 j_2 J} = C\ (j_1 j_2 m_1 m_2 ; JM)$$

When $S_2 = \lambda_2 = 0$ and $S_1 = \frac{1}{2}$ we obtain:

$$< JM, L\ 1/2 | JM\lambda_i > \ = \ (-)^{\lambda_1 + 1/2} \ C^{J\ 1/2\ L}_{-\lambda_i \lambda_i 0} \tag{4}$$

$$< JMj\lambda \ | JM, L' j > \ = \ (-1)^{j+\lambda} \ C^{J\ j\ L'}_{-\lambda\ \lambda\ 0} \tag{5}$$

Using the relations 2), 3), 4) and 5) in 1) we obtain

$$< \pi_1(\Lambda\pi_2) | T | kP >_{M_i M_f^*} = \sum_{JLL'} \sum_{\lambda_i \lambda} < \bar{q}_1 \bar{q}_1^* M_f^* | JMj\lambda > < JMj\lambda | JM; L' j > \tag{1'}$$

$$\cdot \ T^{JLL'}_{j\lambda}(W, w_1) < JM; L\ 1/2 | JM\lambda_i > < JM\lambda_i | \bar{q}_i M_i >$$

$$= \frac{1}{2\pi} \frac{4W\sqrt{4w_1}}{\sqrt{q_i q_1 q_1^*}} \sum_{JLL'} \sqrt{\frac{2J+1}{2}} \ T^{JLL'}_{j\ell}(W, w_1) \sqrt{\frac{2J+1}{2}}$$

$$\cdot \sum_{\lambda} (-1)^{1/2 + M_i} (-1)^{j+\lambda} \ C^{J 1/2 L}_{-M_i M_i 0} \ C^{J j L'}_{-\lambda \lambda 0} \ C^{\ell 1/2 j}_{\nu M_f^* \lambda} \ Y^{\ell}_{\nu}(\theta_1^*, \varphi_1^*) d^J_{M_i \lambda}(\theta_1)$$

The second form above comes from simplification of the following expressions:

a) $< \bar{q}_1 \bar{q}_1^* M_f^* | JMj\lambda > \ = \ < \bar{q}_1^* M_f^* | j\ell\lambda > < \bar{q}_1 \lambda | JM\lambda >$

where (ℓ) is the orbital state in the decay of the subsystem $(\Lambda\pi_2)$. This is a product of two wave functions in the final state, one in the 3 c.m. the other in the rest frame of $(\Lambda\pi_2)$ subsystem . b) $< JM\lambda_i | q_i M_i >$ which is the projection of the initial state on some helicity state.

From the properly normalized helicity eigenstates[16] we find the product b) $= \sqrt{\frac{4W}{q_i} \quad \frac{2J+1}{4\pi}} \ \delta_{M\lambda_i} \ \delta_{M_i \lambda_i}$

In a) M_f^* is the z-component of Λ-spin in the Λ rest frame where the z-axis is taken parallel to the $(\Lambda\pi_2)$ line of flight in 3 c.m. and x-axis parallel to the $(\Lambda\pi_2)$ production plane; λ is the helicity of $(\Lambda\pi_2)$ subsystem in 3 c.m.

The proper coordinate system in which to describe the Λ-spinor is the Λ-rest frame, with a quantization axis along the vector that transforms the Λ to its rest frame. Thus to evaluate the first part of a) we rotate the spin state of the Λ in order to describe it in terms of the proper spin eigenfunctions, we obtain:

$$< \bar{q}_1^{*} \, M_f^{*} | j \; \ell \; \lambda > \; = \sqrt{\frac{4W_1}{q_1^{*}}} \; C^{\ell \;\; 1/2 \;\; j}_{\nu \;\; M_f^{*} \;\; \lambda} \;\; Y^{\ell}_{\nu} \, (\theta_1^{*}, \varphi_1^{*})$$

To evaluate the second part of a) we project the helicity state of $(\Lambda\pi_2)$ along the $\bar{q}_1$ direction and obtain: (Reference 16, Appendix 1-A)

$$< \bar{q}_1 \lambda | J \; M \; \lambda > \; = \sqrt{\frac{2J+1}{4\pi} \;\; \frac{4W}{q_1}} \;\; D^{J}_{M\Lambda} \, (0, \theta_1, 0)$$

where θ_1 is the production angle of $(\Lambda\pi_2)$ subsystem in 3 c.m. with respect to the incoming direction as z-axis. θ_1^{*}, φ_1^{*} are the polar coordinates of the Λ in the $(\Lambda\pi_2)$ rest frame, with z-axis taken along the $(\Lambda\pi_2)$ line of flight in 3 c.m. and x-axis in the production plane

$D^J_{mm'}(\alpha,\beta,\gamma)$ is the angular momentum rotation operator $D^J_{mm'}(0,\beta,0) = d^J_{mm'}(\beta)$.

It is seen that the angular dependence in the amplitude equation (1′) is in terms of θ_1, the $(\Lambda\pi_2)$ subsystem production angle, and $(\theta_1^{*}, \varphi_1^{*})$ the polar coordinates of the Λ in the $(\Lambda\pi_2)$ rest frame with respect to $(\Lambda\pi_2)$ line of flight. It must be remembered that, implicit in the development of the above, the spin of the Λ in the final state is quantized with the $(\Lambda\pi_2)$ line of flight as z-axis, and the initial proton spin along the incoming direction.

At this point a transformation can be made to the coordinate system $(\xi\eta\zeta)$ that we chose as most convenient in Chapter III, i.e. ζ-axis as the normal to the 3-particle plane $(\zeta = \bar{\pi}_1 \times \bar{\pi}_2)$, $(-\xi)$ axis as bisector of (π_1, π_2) angle. We must transform the spinors and spherical harmonics by the use of angular momentum rotation operators $D^J_{mm'}(\alpha, \beta, \gamma)$.[16] We require this transformation to produce an amplitude in which all spins are quantized along the ζ-axis and in which the independent variables are the five variables we chose in Chapter III-B namely: Θ, Φ, w_1, w_2 and the angle of rotation around the incoming direction. We obtain:

$$< \pi_1(\Lambda\pi_2)|T|KP>_{\mu_i\mu_f} = \frac{1}{2\pi} \sum_{JLL'j\ell} \sqrt{\frac{2J+1}{2}} \; \frac{4W}{\sqrt{q_i}} \sqrt{\frac{4w_1}{q_1 q_1^*}} \; T^{JLL'}_{j\ell}(W, w_1) \, f^{JLL'j\ell}_{\mu_i\mu_f}(\theta_1^*, \frac{\theta_{12}}{2})$$

$$\cdot \exp(i\mu_f \, \Omega_1)$$

where μ_i, μ_f are the projection of proton and Λ spins along the ζ-axis, Ω_1, is a relativistic rotation of Λ spinor obtained when a Lawrentz transformation (L.T.) takes Λ from 3 c.m. to Λ-rest frame on one hand, and L.T. of Λ from 3 c.m. to $(\Lambda\pi_2)$ rest frame then to Λ-rest frame on the other.[24] This rotation is needed in principle in order to make the amplitude symmetric under exchange of π_1, π_2.

As given by Stapp[24] $\sin|\Omega_1| = \dfrac{(\bar{\beta}_1^* \gamma_1^* \times \bar{\beta}_1 \gamma_1)(1+\gamma_1^* + \gamma_1 + \gamma_\Lambda)}{(1+\gamma^*)(1+\gamma_1)(1+\gamma_\Lambda)}$

where $\gamma = \sqrt{1+\beta^2\gamma^2}$ as usual and $\bar{\beta}_1$ is the velocity of $(\Lambda\pi_2)$ in 3 c.m., $\bar{\beta}_1^*$ is the velocity of Λ in the $(\Lambda\pi_2)$ rest frame, γ_1 is for $(\Lambda\pi_2)$ system in 3 c.m. and γ_Λ is for Λ in the 3 c.m. system. (At incident K^- momentum of 1000 MeV/c and for $Y_1^*(1385)$ production, the momentum of the spectator pion in 3 c.m. is 339 MeV/c. Thus $\gamma_1 = 1.03$, $\beta_1\gamma_1 = .25$, $\gamma_1^* = 1.017$,

$\beta_1^* \gamma_1^* = .18$, and γ_Λ has the largest value of 1.096. Thus, $|\Omega_1| = .0217$ radians. The effect of this rotation will be ignored.) By definition we have written:

$$f^{JLL'j\ell}_{\mu_i\mu_f}(\theta_1^*, \frac{\theta_{12}}{2}) = \sqrt{\frac{2J+1}{2L+1}} \sum_{\lambda>0} \sum_{M_f^*} \sum_K \sum_m (-1)^{1/2+j} C^{JjL'}_{-\lambda\lambda 0} \left[1+(-1)^{L+m+1}\right] \cdot$$

$$\cdot\ C^{\ell\,1/2\,j}_{\nu M_f^* \lambda}\ C^{1/2\,J\,K}_{M_f^*\,-\lambda-\nu}\ C^{1/2\;J\;K}_{\mu_f\,m-\mu_f\,m}\ d^K_{m,-\nu}\left(\frac{\pi}{2}\right) (-i)^\nu P^\ell_\nu (\theta_1^*)$$

$$\cdot\ C^{J\quad 1/2\quad L}_{m-\mu_f\ \mu_i\ m-\mu_f+\mu_i}\ Y^L_{m+\mu_i-\mu_f}(\Theta,\Phi) \exp\left(i\, m \frac{\theta_{12}}{2}\right)$$

where λ, K, M_f^* are now dummy indices, θ_1^* is the decay angle of $(\Lambda\pi_2)$ system in its rest frame, θ_{12} is the angle between Y^{*+} and Y^{*-} in 3 c.m. Θ,Φ are polar coordinates of the incoming direction in the $\xi\eta\zeta$ system. The cosine of θ_1^* is equivalent to one of the coordinates of the Dalitz plot. The expression in square brackets is a parity conservation coefficient; $d^K_{m\,\nu}$ is a reduced angular momentum rotation matrix element. The rest of the symbols are defined previously.

If we now restrict the $(\Lambda\pi_2)$ subsystem to be $Y_1^*(1385)$ i.e. allowed values of $\ell=1$, $j=3/2$ and parity determined by restricting the values of ν; then $f^{JLL'\,3/2\,1}_{\mu_i\mu_f}$ can be reduced considerably, and it takes a form that can be easily used in a program for digital computer.

By inspection of the above and using the properties of the spherical harmonics and Clebsh-Gordan coefficients we find:

$$f^{JLL'j\ell}_{\mu_i\mu_f}(\theta^*, \theta_{12}) = (-)^{\mu_i-\mu_f} \left\{ f^{JLL'j\ell}_{-\mu_i-\mu_f}(\theta^*, \theta_{12}) \right\}^*$$

where the * on the curled bracket implies complex conjugation. For other properties see Reference 16. We give a table of values for the function $f^{JLL'3/2 1}_{\mu_i\mu_f}(\theta,\theta_{12})$ that correspond to $Y_1^*(1385)$ as intermediate state. Table B-I contains values of the function for $\mu_i=-1/2$, $\mu_f=1/2$ (SF) and $\mu_i=1/2$, $\mu_f=1/2$ (NSF). The dependence on the angle θ_{12} (angle between the two final-state pions in 3 c.m.) is omitted. The arguments of $Y_\ell^m(\Theta,\Phi)$ which are omitted in the table are the polar coordinates of the incoming K^- direction in the $\xi\eta\zeta$ coordinate axes.

C. Centrifugal Barrier Effects and Parameters of $Y_1^*(1385)$ Resonance Shape

The rate for the decay of a bound state into two particles depends on centrifugal barrier factors which are different for different values of the orbital angular momentum state (ℓ) between the decay products. Blatt and Weisskopf (Theoretical Physics, Wiley (1958) p. 361) give these factors v_ℓ as:

$$v_0 = 1$$

$$v_1 = \frac{(kr)^2}{1+(kr)^2}$$

$$v_2 = \frac{(kr)^4}{9+3(kr)^2+(kr)^4}$$

$$v_3 = \frac{(kr)^6}{225+45(kr)^2+6(kr)^4+(kr)^6}$$

where ($\hbar k$) is the relative momentum of the decay products of a resonant state and r is an interaction radius, usually of the order of a Fermi. We use these factors for introducing centrifugal barrier in factoring T in Chapter III Section B.

The width of a resonance into a certain channel may be parameterized as (Blatt and Weisskopf p. 390 op. cit)

$$\Gamma \sim \gamma\ (kr'v_\ell)$$

Table B-I. Values of the function $f_{\pm 1/2,1/2}(\theta,\theta_{12}=0)$

NSF: $f_{1/2,1/2}$; SF: $f_{-1/2,1/2}$

Wave		
PP1	NSF	$.2887\ (i\sin\theta^{*}+2\cos\theta^{*})Y_{0}^{1}$
	SF	$.4083\ (i\sin\theta^{*}+2\cos\theta^{*})Y_{-1}^{1}$
SD1	NSF	0
	SF	$-\ (.5i\sin\theta^{*}+\cos\theta^{*})Y_{0}^{0}$
DS3	NSF	$-\sqrt{2}\mathrm{x}.2739\{(i\sin\theta^{*}+\cos\theta^{*})Y_{-1}^{2}+(i\sin\theta^{*}-\cos\theta^{*})Y_{1}^{2}\}$
	SF	$-\sqrt{2}\ \{.5478(i\sin\theta^{*}+\cos\theta^{*})Y_{-2}^{2}+.2236(i\sin\theta^{*}-\cos\theta^{*})Y_{0}^{2}\}$
PP3	NSF	$-.1291\ (5i\sin\theta^{*}+\cos\theta^{*})Y_{0}^{1}$
	SF	$.0913\ \{(5i\sin\theta^{*}+\cos\theta^{*})Y_{-1}^{1}+3(i\sin\theta^{*}-\cos\theta^{*})Y_{1}^{1}\}$
DD3	NSF	$.2738\ \{\cos\theta^{*}Y_{-1}^{2}-(2i\sin\theta^{*}+\cos\theta^{*})Y_{1}^{2}\}$
	SF	$.5477\ \cos\theta^{*}Y_{-2}^{2}-.2236(2i\sin\theta^{*}+\cos\theta^{*})Y_{0}^{2}$
PF3	NSF	$.3873\ \cos\theta^{*}Y_{0}^{1}$
	SF	$.2739\ \{(2i\sin\theta^{*}+3\cos\theta^{*})Y_{1}^{1}-\cos\theta^{*}Y_{-1}^{1}\}$
DD5	NSF	$.1195\ \{(2i\sin\theta^{*}+\cos\theta^{*})Y_{1}^{2}-(5i\sin\theta^{*}+\cos\theta^{*})Y_{-1}^{2}\}$
	SF	$.2988\ \{(-i\sin\theta^{*}+\cos\theta^{*})Y_{2}^{2}-(i\sin\theta^{*}+.5\cos\theta^{*})Y_{0}^{2}+(i\sin\theta^{*}+.2\cos\theta^{*})Y_{-2}^{2}\}$
DG5	NSF	$-.0732\ \{(i\sin\theta^{*}+4\cos\theta^{*})Y_{1}^{2}+(i\sin\theta^{*}-4\cos\theta^{*})Y_{-1}^{2}\}$
	SF	$.0896\ (i\sin\theta^{*}+4\cos\theta^{*})Y_{0}^{2}+.0366(i\sin\theta^{*}-4\cos\theta^{*})Y_{-2}^{2}$
FP5	NSF	$\sqrt{3}\ \{-.2315(i\sin\theta^{*}+\cos\theta^{*})Y_{-2}^{3}+.2535\cos\theta^{*}Y_{0}^{3}+.2315(i\sin\theta^{*}-\cos\theta^{*})Y_{2}^{3}\}$
	SF	$\sqrt{3}\ \{-.5669(i\sin\theta^{*}+\cos\theta^{*})Y_{-3}^{3}+.2928\cos\theta^{*}Y_{-1}^{3}+.1464(i\sin\theta^{*}-\cos\theta^{*})Y_{1}^{3}\}$

Table B-I. continued

Wave		
FF5	NSF	$.0472\,(11i\sin\theta^*+4\cos\theta^*)Y_2^3-.0518(5i\sin\theta^*+4\cos\theta^*)Y_0^3+.0472(-i\sin\theta^*+4\cos\theta^*)Y_{-2}^3$
	SF	$.0299\,(11i\sin\theta^*+4\cos\theta^*)Y_1^3-.0598(5i\sin\theta^*+4\cos\theta^*)Y_{-1}^3+.1157(-i\sin\theta^*+4\cos\theta^*)Y_{-3}^3$
FF7	NSF	$-.1056\,(5i\sin\theta^*+\cos\theta^*)Y_{-2}^3+.1157(3i\sin\theta^*+\cos\theta^*)Y_0^3-.1056(i\sin\theta^*+\cos\theta^*)Y_2^3$
	SF	$-.3018\,(-i\sin\theta^*+\cos\theta^*)Y_3^3+.1670(i\sin\theta^*+\cos\theta^*)Y_1^3-.1002(3i\sin\theta^*+\cos\theta^*)Y_{-1}^3+.0431(5i\sin\theta^*+\cos\theta^*)Y_{-3}^3$
GD7	NSF	$-.3951\,\left[(i\sin\theta^*-\cos\theta^*)Y_3^4+(i\sin\theta^*+\cos\theta^*)Y_{-3}^4\right]+.1494\left[(i\sin\theta^*-3\cos\theta^*)Y_1^4+(i\sin\theta^*+3\cos\theta^*)Y_{-1}^4\right]$
	SF	$-.2113\,\left[(i\sin\theta^*-\cos\theta^*)Y_2^4-(i\sin\theta^*+3\cos\theta^*)Y_{-2}^4\right]+.1336(i\sin\theta^*-3\cos\theta^*)Y_0^4-.5589(i\sin\theta^*+\cos\theta^*)Y_{-4}^4$
GG7	NSF	$-.0295\,(16i\sin\theta^*+5\cos\theta^*)Y_3^4+.1670(2i\sin\theta^*+\cos\theta^*)Y_1^4-.0334(4i\sin\theta^*+5\cos\theta^*)Y_{-1}^4+.0295(-2i\sin\theta^*+5\cos\theta^*)Y_{-3}^4$
	SF	$-.0157\,(16i\sin\theta^*+5\cos\theta^*)Y_2^4+.5976(2i\sin\theta^*+\cos\theta^*)Y_0^4-.0472(4i\sin\theta^*+5\cos\theta^*)Y_{-2}^4+.8333(-2i\sin\theta^*+5\cos\theta^*)Y_{-4}^4$
FH7	NSF	$.0472\,(2i\sin\theta^*+5\cos\theta^*)Y_2^3-.2588\cos\theta^*Y_0^3+.0472(-2i\sin\theta^*+5\cos\theta^*)Y_{-2}^3$
	SF	$.4050\,(4i\sin\theta^*+5\cos\theta^*)Y_3^3-.2241(2i\sin\theta^*+5\cos\theta^*)Y_1^3+.6723\cos\theta^*Y_{-1}^3-.0579(-2i\sin\theta^*+5\cos\theta^*)Y_{-3}^3$

with v_ℓ as above, r' is of the order of the nucleon radius, and γ is a factor which depends on energy and interior properties of the resonance.

For the $Y_1^*(1385)$ we may then write

$$\Gamma \sim \gamma \; \frac{(kr)^3}{1+(kr)^2}$$

If we measure r in units of pion radius and use the momentum (p) of the decay pion ($Y_1^* \rightarrow \Lambda\pi$) in the Y_1^* rest frame, then

$$kr \sim \frac{p}{\hbar} \; \frac{a\hbar}{\mu c} = \frac{p}{\mu c} \; a = a\eta \text{ (a: unknown parameter)}$$

and

$$\Gamma \sim \gamma \; \frac{(a\eta)^3}{1+(a\eta)^2} = \frac{A_1 \eta^3}{1+A_2\eta^2}$$

which is the parameterization for the width of the $Y_1^*(1385)$ thus making γ independent of energy which is plausible for a narrow resonance.

To find values for A_1 and A_2 we have used data ($K^- p \rightarrow Y_1^* + \pi \rightarrow \Lambda\pi^+\pi^-$) at K^- momentum (1.45 - 1.6) GeV/c from D. O. Huwe[27] (Ph.D. Thesis, unpublished UCRL-11291 (1964)). We chose high energy data because interference effects that may change the shape and position of the resonance peak are smaller at 1.6 GeV/c than at our momenta (.85 - 1.11 GeV/c).

We fitted the ($Y_1^{*+} + Y^{*-}$) peak of Huwe's data by minimizing χ^2 and varying A_1, A_2, and the mass of the resonance and the contribution of 3-body phase space background. We get ~10% probability for the best fit, which gives the following values of the parameters

A_1 = 0.0143 BeV

A_2 = 0.6395

Mass = 1.3837 BeV

Background = 31%

The value of A_2 implies a radius of interaction $(r) \simeq 1.1$ Fermi. For representative values from the fit, we give the value of the full width:

at Y_1^* mass of 1.367 BeV $\Gamma = .032$ BeV

at 1.387 $\Gamma = .040$ BeV

ACKNOWLEDGMENTS

I would like to thank Dr. Robert W. Birge for interesting me in High Energy Physics and for his constant encouragement, and Professor Robert P. Ely, Jr., for his guidance and many stimulating discussions throughout the progress of this work. The early part of this experiment was carried out in collaboration with Dr. James Louie and many discussions with him have been invaluable, and discussions with Nathan Jew and Dr. Wesley Smart have been fruitful in removing many obstacles. The conscientious and untiring effort of the scanners and measurers of the Powell-Birge group under the supervision of Wes Weber and Charlotte Scales were invaluable and the services of the Data Handling group were quite essential for the carrying out of this work.

I very much like to thank Professor G. Valladas for his helpful comments concerning the model used in this analysis.

I am grateful to Mrs. Sandra Paciotti for a fine and beautiful job in typing this manuscript and to Miss V. LaLonde for her help in preparing the diagrams.

My deep thanks to my parents and grandparents for their patient understanding and advice throughout my graduate school years.

This work was done under the auspices of the U. S. Atomic Energy Commission.

REFERENCES AND FOOTNOTES

1. R. B. Bell, R. W. Bland, M. G. Bowler, J. L. Brown, R. P. Ely, S. Y. Fung, G. Goldhaber, A. A. Hirata, J. A. Kadyk, J. Louie, J. S. Sahouria, V. H. Seeger, W. M. Smart, G. H. Trilling and C. T. Murphy, A Variable Momentum Separated $K^{\pm}$ Beam at the Bevatron, in Proceedings of the XIIth International Conference on High Energy Physics, Dubna, USSR, 1964, (Atomizdat, Moscow, 1966), Vol. I, p. 546.

1a. O. Chamberlain, K. M. Crowe, D. Keefe, L. T. Kerth, A. Lemonick, T. Maung and T. F. Zipf, Phys. Rev. 125, 1696 (1962); E. F. Beal, W. Holley, D. Keefe, L. T. Kerth, J. J. Thresher, C. L. Wang and W. A. Wenzel, Proceedings of the 1962 International Conference on High Energy Physics, CERN, Geneva, Switzerland (1962) p. 368. A. Barbaro-Galtieri, A. Hussain and R. D. Tripp, Phys. Letters 6, 296 (1963).

2. The (FSD) is a computer controlled instrument which utilizes a fast-moving spot of light to digitize coordinates of points on preselected tracks on bubble chamber film by systematically sweeping the plane of the film.

3. J. Louie and J. S. Sahouria, Powell-Birge Group (LRL) note PB-1042.

4. B. Rossi, High Energy Particles, Prentice-Hall (1952), Chapter 2.

5. F. Crawford, Use of Delta-Rays to Determine Particle Velocities, LRL, UCID-241 (1957).

6. For errors in the measurement of track curvatures see Reference 4 and G. Groetzinger, M.J. Berger and F. L. Ribe, Phys. Rev. 77, 584 (1950) or W. T. Scott and H. S. Snyder, Phys. Rev. 78, 223 (1950).

7. A. H. Rosenfeld, N. Barash-Schmidt, A. Barbaro-Galtieri, L. R. Price, M. Roos, P. Soding, W. M. Willis and C. G. Wohl, Rev. Mod. Phys. 40, 77 (1968).

7a. J. Louie, Lawrence Radiation Laboratory, Powell-Birge Group, Private Communication.

8. R. L. Cool, G. Giacomelli, T. F. Kycia, B. A. Leontic, K. K. Li, A. Lundby and J. Teiger, Phys. Rev. Letters 16, 1228 (1966).

9. J. L. Brown, Lawrence Radiation Laboratory, Trilling-Goldhaber Group, Technical Note TGT-29 (unpublished).

10. R. Armenteros, M. Ferro-Luzzi, D. W. G. Leith, R. Levi-Setti, A. Minten, R. D. Tripp, H. Filthuth, V. Hepp, E. Kluge, H. Schneider, R. Barloutaud, P. Grant, J. Meyer and J. P. Porte, Zeit. fur Physik 202, 486 (1967).

11. A. Rosenfeld and W. Humphry, Annual Rev. of Nucl. Sci. 13, 103 (1963).

12. S. S. Fung, An Analysis of Y_1^* Production by 1.15 BeV/c K^- Beam, Ph.D. Thesis, UCRL-11485, 1963.

13. R. H. Dalitz and D. H. Miller, Phys. Rev. Letters 10, 562 (1961).

14. M. Olsson and C. R. Yodh, Phys. Rev. Letters 10, 353 (1963).

15. S. Bergia, F. Bonsignori and A. Stanghellini, Nuovo Cimento 16, 1073 (1960).

16. B. Deler and G. Valladas, Nuovo Cimento 45, 560 (1966).

16a. For a very short treatment similar to that of reference 16 see: High Energy Physics, Lectures delivered at Les Houches during the 1965 session of the Summer School of Theoretical Physics with a grant from NATO; C. DeWitt and M. Jacob editors, Gordon and Breach Science Publishers, Lecture by J. D. Jackson, p. 348.

17. N. Byers and S. Fenster, Phys. Rev. Letters 11, 52 (1963).

18. J. Button-Shafer, Phys. Rev 150, 1364 (1966).

19. S. M. Berman and M. Jacob, Spin and Prity Analysis in Two-Step Decay Processes, Stanford Linear Accelerator, SLAC Report-43, 1965, (unpublished).

20. P. E. Schlein, D. D. Carnomy, G. M. Pjerrou, W. E. Slater, D. H. Stork, and H. K. Ticho, Phys. Rev. Letters 11, 167 (1963).

21. S. M. Berman and M. Jacob, Phys. Rev. 139, 1023 (1965).

22. For the sake of completeness we mention the contributions $K^-p \rightarrow \Lambda(\pi^+\pi^-) \rightarrow \Lambda\pi^+\pi^-$ signifying π-π final state interaction or ρ-production; and the simple s-wave phase space where there is no final state interaction between any combination of the final three particles. At the highest energy in this experiment (invariant mass 1.845 BeV) we are at the threshold of $\Lambda\rho$ production. We shall show in Chapter IV that the two processes mentioned in the text are the main contributors to the reaction considered in our energy region.

23. For properties of helicity states see M. Jacob and G. C. Wick, Ann. of Phys. 7, 404 (1959).

24. C. Møller, The Theory of Relativity, Oxford University Press (1951) p. 56; H. P. Stapp, Phys. Rev. 103, 425 (1957).

25. H. L. Kraybill, D. L. Stonehill, B. Deler, W. Laskar, J. P. Merlo, G. Valladas, and G. W. Tautfest, Phys. Rev. Letters 16, 863 (1966).

26. University of California LRL Berkeley Computer Library, ZOEOVARM-F IV (unpublished); W. C. Davidon, Variable Metric Method For Minimization, Argonne National Laboratory (ANL 5990 Rev. 1959).

27. D. O. Huwe, Study of the Reaction $K^-p \rightarrow \Lambda\pi^+\pi^-$ from 1.2 to 1.7 BeV/c, (Ph.D. Thesis) UCRL-11291, 1964.

28. R. Socolow and S. Coleman, Phys. Rev. 135, B1451 (1964).

29. B. Deler, J. P. Merlo, G. W. Tautfest and G. Valladas, in Proceedings of the XIII International Conference on High Energy Physics, Berkeley 1966.

30. A. Messiah, Quantum Mechanics, Vol. II, John Wiley and Sons (1962).

31. M. E. Rose, *Elementary Theory of Angular Momentum*, John Wiley and Sons (1957).

32. If we follow the sequence of Euler angles rotations described in Reference 30, p. 524 and Reference 31, p. 69, (see also Fig. 11 Chapter IV of this paper) then one can write the following:

$$D^{1/2}_{m'm}(\alpha,\beta,\gamma) = \begin{pmatrix} e^{-i/2(\alpha+\gamma)}\cos\beta/2 & -e^{i/2(\alpha-\gamma)}\sin\beta/2 \\ e^{-i/2(\alpha-\gamma)}\sin\beta/2 & e^{i/2(\alpha+\gamma)}\cos\beta/2 \end{pmatrix}$$

the values of m′ are +1/2 and -1/2 going down and m = +1/2, -1/2 going from left to right.

33. There have been many resonant states found in the K^-p reaction near the mass region 1700 MeV. Reference 7 gives the following $1/2^-$ $Y_0^*(1670)$, $3/2^-$ $Y_0^*(1690)$, $3/2^-$ $Y_1^*(1660)$, and $Y_1^*(1690)$ with spin and parity not well-known.

34. R. W. Birge, R. P. Ely, G. E. Kalmus, A. Kernan, J. Louie, J. S. Sahouria, and W. M. Smart, The Spin and Parity of the $Y_0^*(1815)$ and the $Y_1^*(1765)$, in *Proceedings of the Second Topical Conference on Resonant States, Ohio University, Athens, 1965*, edited by B. A. Munir p. 296; W. M. Smart, Phys. Rev. 169, 1330 (1968); R. Armenteros, M. Ferro-Luzzi, D. W. G. Leith, R. Levi-Setti, A. Minten, R. D. Tripp, H. Filthuth, V. Hepp, E. Kluge, H. Schneider, R. Barloutaud, P. Granet, J. Meyer and J. P. Porte, Nuclear Phys, B3 (1967) p. 592-600; R. B. Bell, R. W. Birge, Y. L. Pan and R. T. Pu, Phys. Rev. Letters 16, 203 (1966).

35. The values given in the text for the cross-sections of these resonances correspond to (33.4 ± 5.0)% elasticity for the $Y_1^*(1765)$ and (60.0 ± 6.0)% for the $Y_0^*(1820)$. The published values for elasticities (see Reference 7) range from 34% to 60% for the $Y_1^*(1765)$ and from 63% to 80% for the $Y_0^*(1820)$.

36. R. Armenteros, P. Baillon, C. Bricman, M. Ferro-Luzzi, D. E. Plane, N. Schmitz, E. Burkhardt, H. Filthuth, E. Kluge, H. Oberlack, R. R. Ross, Barloutaud, P. Granet, J. Meyer, J. P. Porte, J. Prevost, Partial Wave Analysis of the Reaction $K^-p \to \Sigma\pi$ Between 0.6 and 1.0 GeV/c. CERN report D.Ph.II/DP/js 10.7.1968, and The Reactions $K^-p \to K^-p$ and $K^-p \to \bar{K}^0 n$ Between 600 and 1200 MeV/c, CERN/D.Ph.II/ Physics 68-19, 3.9.1968 (to be published).

37. R. Armenteros, M. Ferro-Luzzi, D. W. G. Leith, R. Levi-Setti, A. Minten, R. D. Tripp, H. Filthuth, V. Hepp, E. Kluge, H. Schneider, R. Barloutaud, P. Granet, J. Meyer, and J. P. Porte, Zeit. fur Physik 202, 486 (1967), R. P. Uhlig, G. R. Charlton, P. E. Condon, R. G. Glasser, and G. B. Yodh, Phys. Rev. 155, 1448 (1967).

38. D. V. Bugg, R. S. Gilmore, K. M. Knight, D. C. Salter, G. H. Stafford, E. J. N. Wilson, J. D. Davies, J. D. Dowell, P. M. Hattersley, R. J. Homer, A. W. O'Dell, A. A. Carter, R. J. Tapper, and K. F. Riley, Phys. Rev. 168, 1466 (1968).

FIGURE CAPTIONS

Fig. 1. Typical vee and two-prong event in the 25 inch Hydrogen Bubble Chamber.

Fig. 2A. Missing mass squared histogram in the reaction $K^-p \rightarrow \Lambda\pi^+\pi^-$ + missing mass.

Fig. 2B. Missing mass histogram in the reaction $K^-p \rightarrow \pi^+\pi^-$ + missing mass.

Fig. 3. Resolution of the Λ-Σ^o overlap region.

Fig. 4. Partial cross-section for the reaction $K^-p \rightarrow \Lambda\pi^+\pi^-$.

Fig. 5A. Azimuthal distribution of the lambda line of flight in the laboratory with respect to the beam direction as z-axis.

Fig. 5B. Azimuthal distribution in the laboratory of the lambda decay-pion with the lambda line of flight in the laboratory as z-axis.

Fig. 6. The coordinate axes ξ-η-ζ described in the text, and the orientations of the Y^* production and the 3-particle planes in the overall center of mass system.

Fig. 7. Calculated components of the theoretical Dalitz-plot distribution for the wave FP5 at the K^- beam momentum 1020 MeV/c. The components labled from 1 to 4 correspond to the parameterization described in the text.

Fig. 8. Effect of the iso-spin interference terms on the position of the Y_1^* resonance peak, shown for the wave FP5 at the beam momentum 1058 MeV/c.

Fig. 9A. Decay angular distributions for the Y_1^{*+}(1385) with respect to its line of flight in the overall center of mass system. The smooth curve is from the best solution.

Fig. 9B. Decay angular distributions for the Y_1^{*-}(1385).

Fig. 10. Experimental Dalitz plots.

Fig. 11. Rotations and the Euler's angles $\alpha\ \beta\ \gamma$ needed to calculate the lambda polarization from the model.

Fig. 12A. Experimental lambda polarization, folded about $\hat{\Lambda}\cdot\hat{Z}=0$ and for the range -.8 to +.8 in cosine of the production angle $(K\cdot Y^{*+})$, for the Y_1^{*+} production.

Fig. 12B. The same as Fig. 12A but for the Y^{*-} production.

Fig. 13. Partial cross-sections in millibarn, for the partial waves used in the fitting procedure, obtained from the best solution.

Fig. 14A. Experimental histograms of the events used in the fitting versus the $(\Lambda\pi^+)$ mass-squared, the smooth curve is calculated from the best solution.

Fig. 14B. The same as Fig. 14A but for the $(\Lambda\pi^-)$ subsystem.

Fig. 15A. The experimental production angular distributions for the Y_1^{*+} production used in the fitting procedure; the smooth curves are from the best solution.

Fig. 15B. The same as Fig. 15A but for the Y_1^{*-} production.

LEGAL NOTICE

TECHNICAL INFORMATION DIVISION
LAWRENCE RADIATION LABORATORY
UNIVERSITY OF CALIFORNIA
BERKELEY, CALIFORNIA 94720